nature cell biology

Article

https://doi.org/10.1038/s41556-024-01521-9

Recording morphogen signals reveals mechanisms underlying gastruloid symmetry breaking

Received: 19 October 2023

Accepted: 5 September 2024

Published online: 2 October 2024

Check for updates

Harold M. McNamara [1] ✉, Sabrina C. Solley [2], Britt Adamson [1,2], Michelle M. Chan [1,2] & Jared E. Toettcher [2,3] ✉

Aggregates of stem cells can break symmetry and self-organize into embryo-like structures with complex morphologies and gene expression patterns. Mechanisms including reaction-diffusion Turing patterns and cell sorting have been proposed to explain symmetry breaking but distinguishing between these candidate mechanisms of self-organization requires identifying which early asymmetries evolve into subsequent tissue patterns and cell fates. Here we use synthetic 'signal-recording' gene circuits to trace the evolution of signalling patterns in gastruloids, three-dimensional stem cell aggregates that form an anterior–posterior axis and structures resembling the mammalian primitive streak and tailbud. We find that cell sorting rearranges patchy domains of Wnt activity into a single pole that defines the gastruloid anterior–posterior axis. We also trace the emergence of Wnt domains to earlier heterogeneity in Nodal activity even before Wnt activity is detectable. Our study defines a mechanism through which aggregates of stem cells can form a patterning axis even in the absence of external spatial cues.

Living systems break symmetries to form spatially organized structures across many scales. In the embryo symmetries are often broken by extrinsic cues, which provide a blueprint of positional information to guide developmental programmes[1–3]. Recent advances in stem cell culture have demonstrated that simple aggregates of cells can build embryo-like structures in vitro even without the full complement of embryonic patterning cues[4–7]. Although these 'stembryo' systems do not recapitulate all aspects of normal development, they offer a window into the latent potential of stem cells to self-organize multicellular patterns. How stembryo patterns emerge from signalling interactions between cells remains largely unknown[8]. Understanding the mechanistic basis of stem cell self-organization is ultimately important for interpreting the correspondence between in vitro embryo models and in vivo development.

One of the most important events in embryonic development is the specification of a coordinate system to define the body axes. In vertebrates this occurs during gastrulation where spatial patterns of morphogen ligands (including Wnt, BMP and Nodal) and inhibitors define specific signalling domains (Fig. 1a)[1]. The mouse gastruloid is a stembryo model that breaks symmetry to form a coordinate system, most prominently an anterior–posterior (A–P) axis corresponding to the posterior region of the mouse embryo[4,5,9]. After incubation with the Wnt pathway activator CHIR-99021 (CHIR) between 48 and 72 h after aggregation (haa) gastruloids undergo profound morphological and signalling changes including A–P axis specification and elongation, and the formation of a Brachyury$^+$ posterior pole with active Wnt signalling[9]. It is unknown how the gastruloid generates a posterior pole of Wnt activity in response to a spatially uniform cue (Fig. 1b).

Recent studies of gastruloid self-organization have proposed multiple candidate mechanisms of symmetry breaking. One possibility is that the spherical symmetry of the early cell aggregate is broken

[1]Lewis Sigler Institute for Integrative Genomics, Princeton University, Princeton, NJ, USA. [2]Department of Molecular Biology, Princeton University, Princeton, NJ, USA. [3]Omenn–Darling Bioengineering Institute, Princeton University, Princeton, NJ, USA. ✉e-mail: hmcnamara@princeton.edu; toettcher@princeton.edu

https://doi.org/10.1038/s41556-024-01521-9

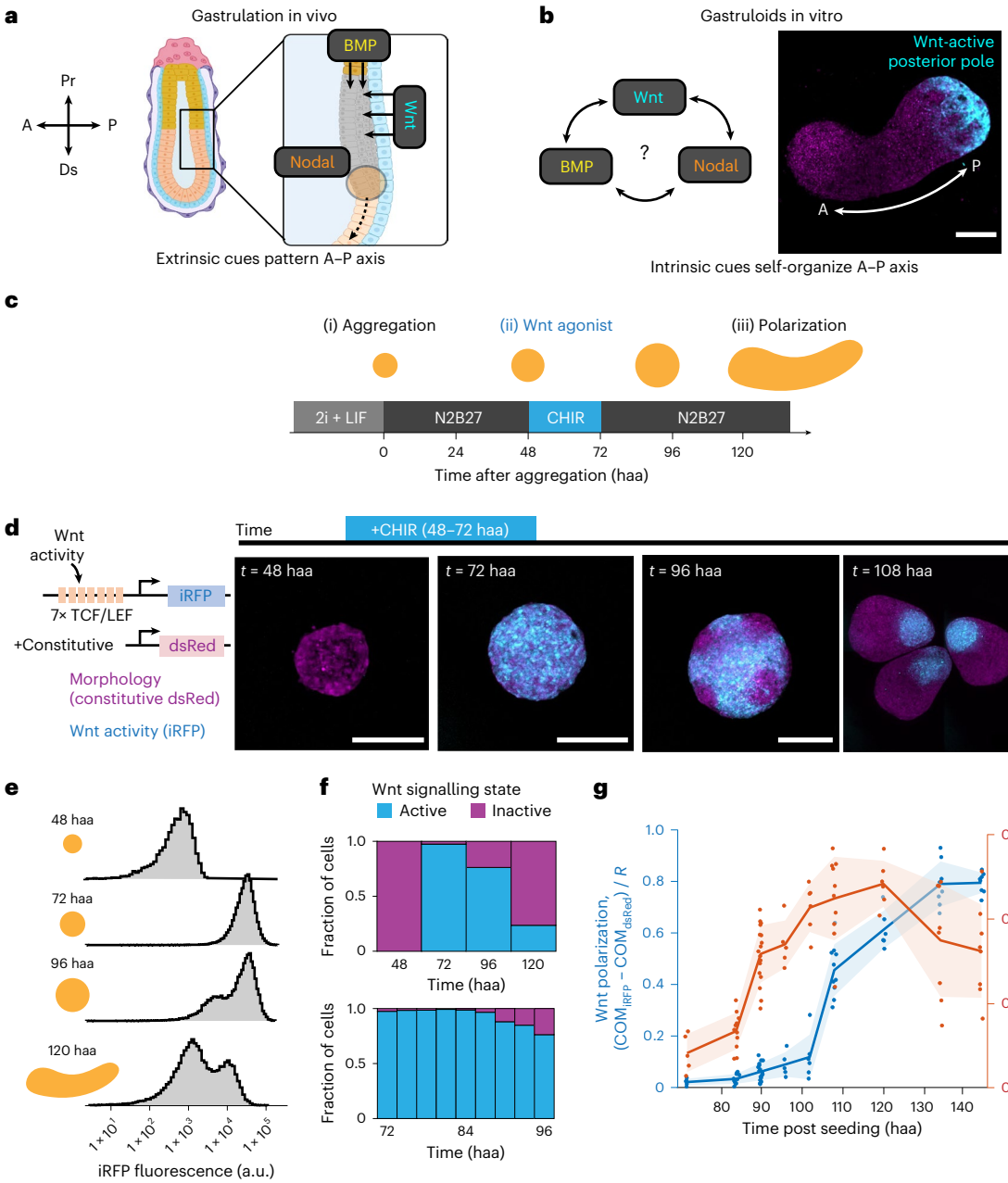

Fig. 1 | Gastruloids self-organize a polarized posterior domain of Wnt activity. **a**, In the mouse embryo gastrulation is initiated by extra-embryonic sources of BMP and Wnt ligands in the posterior epiblast. Nodal activity marks the anterior-most aspect of the resultant primitive streak (that is, the 'node'). Extra-embryonic inhibitors of Wnt and Nodal signalling pattern the anterior epiblast. Pr, proximal; Ds, distal. **b**, The gastruloid self-organizes a posterior domain of Wnt activity without any extrinsic spatial cues. Representative image from six similar gastruloids measured at 120 haa (right). **c**, Protocol used to observe the evolution of Wnt symmetry breaking from a uniform initial condition. To suppress pre-existing heterogeneity in Wnt activity, mESC cultures were maintained in 2i + LIF medium until immediately before gastruloid formation. **d**, Dynamics of Wnt activity patterns during symmetry breaking, as measured by expression of a destabilized near-infrared fluorescent protein (iRFP) downstream of Wnt-sensitive TCF/LEF enhancer sites (left schematic). Samples were fixed at different time points and imaged to measure the spatial distribution of Wnt signalling during polarization. Images represent at least five similar gastruloids measured at each time point. **e**, Flow cytometry was used to measure the levels of Wnt activity in individual cells. The Wnt activity histograms indicate an initially uniform response to Wnt activation with CHIR at 72 h, followed by a bimodal response; a.u., arbitrary units. **f**, Proportion of cells that were Wnt active over time. A Wnt-inactive population was first detectable at time (t) = 90 h. **g**, Levels of heterogeneity and polarization in spatial patterns of Wnt activity during gastruloid morphogenesis (n = 76 gastruloids; see Supplementary Table 3). Heterogeneity is reported as the s.d. of the Wnt reporter normalized to the maximum image intensity and polarization is reported as the distance between the centre of mass (COM) of Wnt activity and morphological images normalized by gastruloid radius R. Quantification indicates an onset of heterogeneity at t = 90 haa (consistent with flow cytometry), followed by polarization at t = 108 haa. The lines and the shaded regions indicate the mean ± s.d., respectively, as a function of time post seeding. Scale bars, 200 µm.

by a reaction-diffusion instability involving signalling ligands and inhibitors (for example, Wnt pathway ligands and the Dkk1 antagonist)[8,10–12] as proposed to explain the formation hair follicles[13], digits[14] and fingerprint patterns[15]. An alternative model involves cell sorting to rearrange cells expressing Wnt at high and low levels (Wnt-high and Wnt-low, respectively) to distinct domains[16], as observed in the formation of somite compartments[7] and the radial polarization of mammary organoids[17]. Distinguishing between these mechanisms is challenging

because patterns that seem consistent with Turing mechanisms may instead be generated by tissue mechanics and cellular rearrangements, and vice versa[18–20]. Ideally, we might distinguish between candidate models by directly linking early signalling states and cell positions to final cell fates over several days of morphogenesis.

Here we engineer synthetic signal-recording circuits to trace the early signalling events that self-organize the gastruloid A–P axis. By permanently labelling cells according to their signalling states within user-defined temporal windows, we link early cell states to future cell fates in both physical and transcriptional space. This approach reveals that early domains of Wnt activity predict the positions of cells along the future A–P axis even before Wnt patterns have polarized. We show that axial polarization proceeds via rearrangement of Wnt-high and Wnt-low cells, and trace the origins of Wnt heterogeneity to pre-existing Nodal and BMP signalling differences. Our results reveal how collections of stem cells can self-organize a patterning axis without extrinsic cues and illustrate a generalizable approach to investigate multicellular symmetry breaking.

Results

Capturing the onset of Wnt heterogeneity and polarization

Gastruloid development is triggered by the addition of CHIR and Wnt activity marks the polarized posterior domain in elongating gastruloids that have broken symmetry. To define the basis of gastruloid symmetry breaking, we therefore began by characterizing the time evolution of Wnt signalling patterns from the initial uniform activation to the final polarized outcome. We generated mouse embryonic stem cells (mESCs) harbouring Wnt-dependent expression of a destabilized infrared fluorescent protein based on a ternary complex factor/lymphoid enhancer factor family (TCF/LEF) enhancer sequence ($P_{TCF/LEF}$–iRFP–PEST; Extended Data Fig. 1a)[21] and constitutive dsRed expression. We also optimized culture conditions to observe the onset of Wnt patterning from an initially uniform state. A standard protocol using LIF-supplemented growth medium led to substantial heterogeneity in Wnt signalling both before and after the 24 h CHIR pulse (Extended Data Fig. 1b,c), consistent with a recent study[22]. In contrast, cells maintained in 2i + LIF medium before gastruloid seeding produced gastruloids in which the Wnt pathway activity progressed from a uniformly high state at 72 haa to a single posterior pole of Wnt activity over time (Fig. 1c,d and Extended Data Fig. 1d). We proceeded with this modified protocol for all subsequent experiments.

We imaged gastruloids harbouring the Wnt transcriptional biosensor at various time points, revealing a progression through uniform, bimodal and polarized pathway activity states. Wnt activity was low in all cells at 48 haa, before the CHIR pulse, but shifted to a uniformly high state by 72 haa (that is, at the end of the CHIR pulse; Fig. 1d). Fragmentation of the Wnt activity pattern into locally ordered domains without global axial polarization was observed by 96 haa (Fig. 1d). Finally, at 108 haa gastruloids exhibited a single coherent domain of Wnt activity that marked the elongating posterior (Fig. 1d). This sharply defined domain of posterior Wnt activity persisted until at least 144 haa (Extended Data Fig. 1d). We separately characterized single-cell Wnt activity levels by flow cytometry on dissociated gastruloid cells (Fig. 1e,f and Extended Data Fig. 1e,f). Consistent with our imaging data, these measurements revealed an initial homogeneously low state at 48 haa, followed by a uniformly high state at 72 haa, which finally shifted to a bimodal distribution with Wnt-high and Wnt-low subpopulations at subsequent time points. Gastruloids imaged at intervals of 6 h pinpointed the onset of heterogeneity between 90 and 96 haa, preceding posterior Wnt polarization by at least 12 h (Fig. 1g and Extended Data Fig. 1d,g).

Recording fate information encoded in morphogen signals

The evolution of Wnt patterning from patchy domains to a single pole could be consistent with either reaction-diffusion patterning in which feedback loops gradually alter the Wnt activity of cells until it forms a single pole or a cell-sorting mechanism where an initial mixture of Wnt-high and Wnt-low cells rearranges to a polarized outcome. We reasoned that these mechanisms could be distinguished by determining the earliest time at which Wnt activity correlates with the anteroposterior position of cells (Fig. 2a). We therefore designed a gene circuit that functions as an AND gate between a candidate signalling pathway and a user-supplied small molecule whose output produces a permanent, heritable fluorescent signal (Fig. 2b). Labelling would thus be restricted to those cells in which a signalling pathway is active during a user-controlled time window. We expressed a destabilized doxycycline (dox)-dependent transcription factor (rtTA) downstream of a 'sentinel enhancer' that responds to a specific pathway of interest[23]. The combined presence of signalling and dox triggers activation of an rtTA-dependent promoter (P_{TetON}) to drive expression of a destabilized Cre recombinase, which in turn results in a permanent change in fluorescent protein expression (dsRed to GFP). Because recordings are inherited by all progeny of labelled cells, they capture differences in proliferation and cell migration between the initial recording and final readout measurement.

We first characterized the performance of a Wnt-responsive signal-recorder circuit (using a TCF/LEF-responsive sentinel enhancer) in cultured mESCs[21]. The circuit demonstrated high sensitivity and specificity to dox and Wnt activity: no detectable GFP labelling was observed when Wnt-recorder cells were incubated in N2B27 medium for 24 h supplemented with either dox or CHIR (Fig. 2c(left)), and the number of GFP-expressing cells remained consistently low (<0.1%) over at least 15 passages of subculture in Wnt-activating 2i medium in the absence of dox. We further characterized the sensitivity of the circuit to each input (dox or Wnt signalling) in the presence of a constant cue from the other input (Extended Data Fig. 2a,b) and found that labelling could be detected for dox concentrations as low as 200 ng ml^{-1} and Wnt3A concentrations as low as 100 ng ml^{-1} (refs. 4,24).

For high-fidelity signal recording, it is important that a brief incubation with dox is sufficient to record the signalling states of cells. We measured the labelling efficiency in mESCs subjected to variable dox incubation times and continuous CHIR treatment (Fig. 2c(right)). A 1 h dox pulse was sufficient to label the majority (68%) of cells; near-complete labelling was achieved after 3 h dox. As a more stringent test, we performed step-up and step-down experiments to measure recording kinetics after an acute change in Wnt activity. We subjected Wnt-recorder mESCs to a 1 h dox pulse at various time points after CHIR stimulation or washout and then measured the final GFP states of the cells after an additional 24 h (Fig. 2d). We observed a delay of 3 h before our labelling circuit reflected the change in Wnt activity, which was probably due to the time required for rtTA expression or removal in cells. By 6 h following the medium change, GFP labelling approached the values obtained in steady-state media conditions. We thus conclude that our signalling-recorder circuits can faithfully resolve signalling dynamics to within a time window of 6 h. For all subsequent experiments, we minimized both the dox concentration (100–200 ng ml^{-1}) and labelling time (1.5–3.0 h) to produce low leakiness recordings of the instantaneous Wnt activity state of cells.

Recombinase recording circuits are modular in design as different sentinel enhancers enable the user to record any transcriptional signal of interest. We developed mESC lines to record Activin and Nodal signalling using the AR8 sentinel enhancer and BMP activity using the IBRE4 sentinel enhancer[23]. All three recorder cell lines (Wnt, Nodal and BMP) could be used to faithfully record ligand-dependent signalling from the appropriate pathway with minimal crosstalk (Fig. 2e and Extended Data Fig. 2c). BMP-recorder cells exhibited some basal GFP conversion that was suppressed by the BMP inhibitor LDN-193189 and thus may reflect autocrine signalling in the culture (Extended Data Fig. 2d). We note that the signal-recording technique 'binarizes' the signalling states of cells such that different signalling intensities may result in different

https://doi.org/10.1038/s41556-024-01521-9

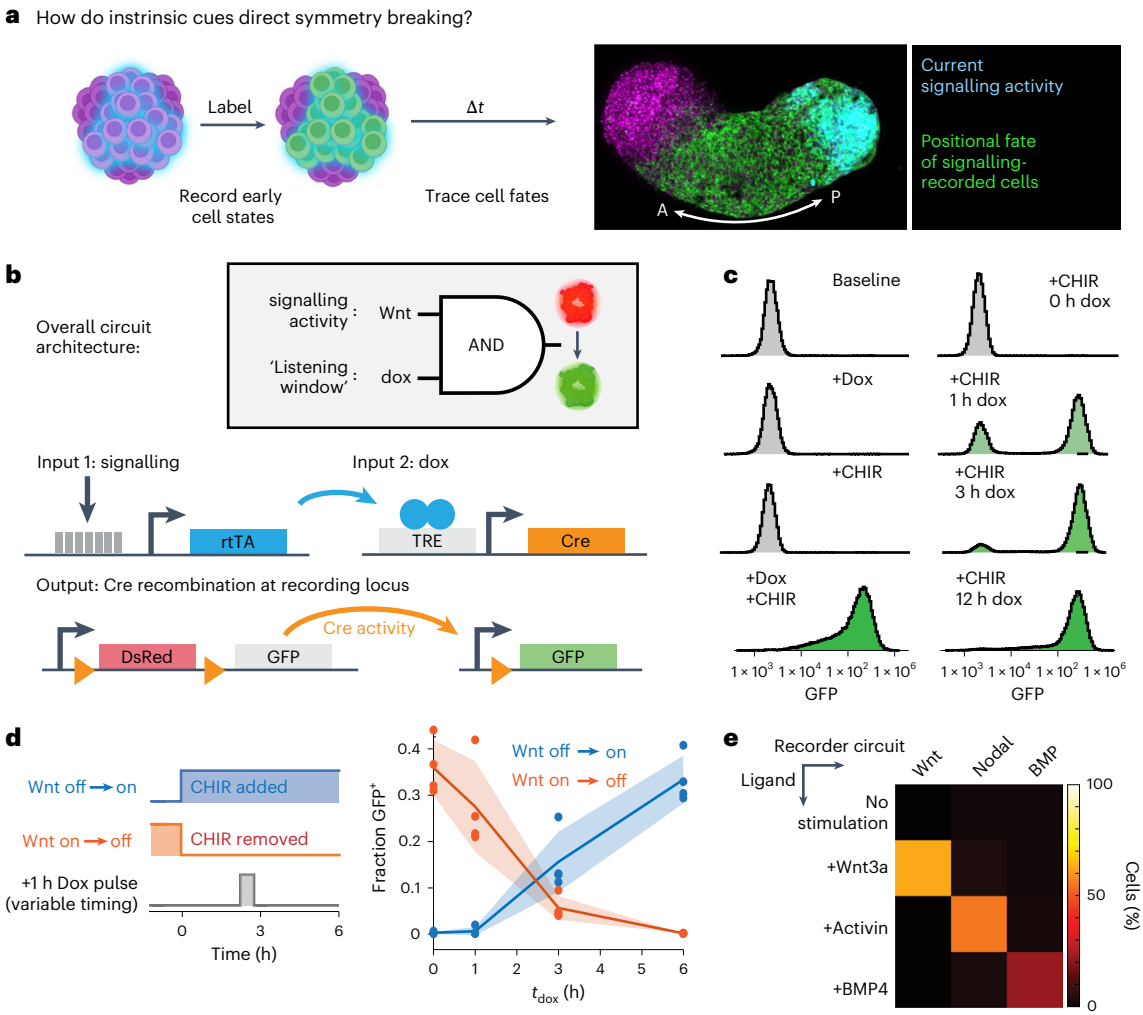

Fig. 2 | Tracing signalling activity in embryonic stem cells using signal-recorder gene circuits. a, Illustration of the signal tracing strategy. To identify which early asymmetries direct self-organization, one would ideally permanently label early cell states so that they can be traced to final cell fates. Intrinsic cues that break symmetry should predict future patterning positions and/or transcriptional cell types. **b**, Schematic of the recording circuit. An upstream transcription factor (rtTA) requires both signalling activity and the addition of small molecules to drive recombinase expression, which in turn irreversibly changes the fluorophore in a 'recording' locus. **c**, Characterization of a clonal Wnt recording the fidelity of a cell line. Incubation with both Wnt-activating CHIR (3 µM) and listening window-defining dox (2 µg ml^{-1}) for 24 h achieves complete GFP labelling (bottom left). Treatment with either CHIR or dox has no detectable labelling (top left). A 1 h recording window is sufficient to achieve efficient labelling (right). **d**, Characterization of switching kinetics of Wnt recorders in response to media changes. A 1 h dox treatment was applied at variable lag times ($\Delta t = t_{dox} - t_0$) following a medium change. The lines and the shaded regions indicate the mean ± s.d., respectively, of three biological replicates per condition. Recorder performance approached steady-state media performance by $\Delta t = 6$ h. **e**, Crosstalk assessment for three separate clonal lines recording Wnt, Activin/Nodal and BMP pathway activity. All recording windows utilized 100 ng ml^{-1} dox and 200 ng ml^{-1} morphogen. Baseline conditions report labelling with only dox in basal medium (N2B27). Pseudocolours indicate the relative proportion of cells labelled with GFP. The recording windows were 6 h for the Wnt and Nodal recorders and 3 h for the BMP recorder to account for differences in sensitivity.

fractions of labelled cells. In summary, our synthetic gene circuits enable mESCs to be labelled based on instantaneous Wnt, Nodal or BMP signalling activity with high fidelity and fine temporal resolution.

Mapping fate information during Wnt symmetry breaking

We applied our Wnt-recording strategy to measure the earliest time at which Wnt activity predicts the future axial position of a cell. We chose nine time points (t_{dox}) to apply 90 min dox pulses to gastruloids, grew them to 134–144 haa and using microscopy observed the final positions of Wnt-recorded cell populations (Fig. 3a and Extended Data Fig. 3). Strikingly, the patchy Wnt activity at 96 haa was already strongly predictive of the posterior position of cells in the elongated gastruloid, despite Wnt activity not yet being axially polarized at that time (Fig. 3b). At later recording times (t_{dox}), Wnt-recorded cells were associated with progressively more posterior positions (Fig. 3b). These data further imply that cells at different final A–P positions also receive different overall durations of Wnt signalling (Extended Data Fig. 3e,f). We thus concluded that 96 haa gastruloids already contain a 'hidden' A–P axis, with the Wnt activity states of cells determining their future axial position. Importantly, this observation begins to constrain candidate models for symmetry-breaking polarization. Because Wnt-high cells at 96 haa are not yet polarized but will contribute exclusively to the future posterior domain, polarization cannot be explained by a reaction-diffusion instability that resolves to a single pole before it encodes posterior information. Instead, our data are consistent with an alternative model: that cell movements rearrange Wnt-active and Wnt-inactive cells into distinct anterior and posterior domains.

Symmetry breaking is not simply a morphological process—embryos also must break transcriptional symmetries to differentiate into specialized cell types. To test whether the Wnt signalling states at

https://doi.org/10.1038/s41556-024-01521-9

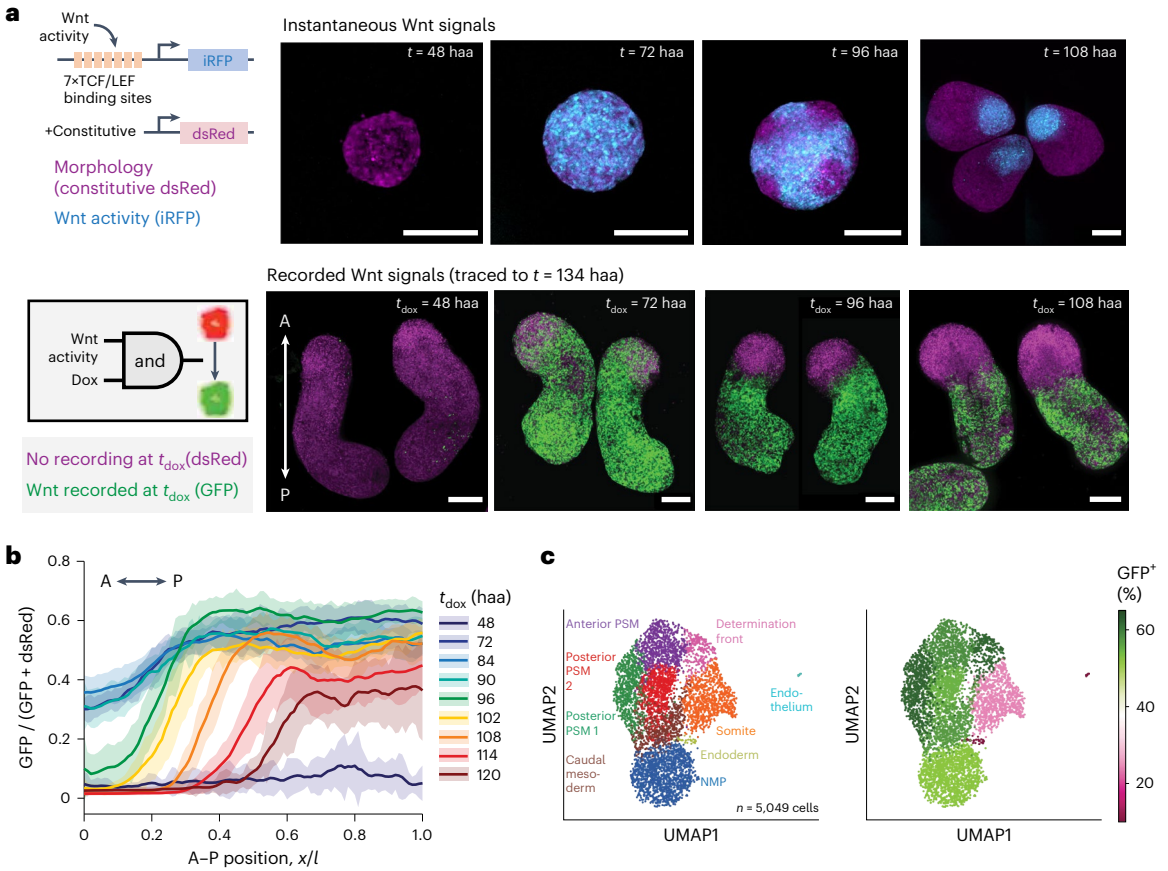

Fig. 3 | Recorded Wnt signalling histories identify the critical time window for specifying the future position and fate of cells. a, Dynamics of early Wnt activity patterns during symmetry breaking (top). Tracing these early Wnt activity to final A–P patterning fates with a Wnt-recording circuit (bottom). Wnt activity was recorded with dox treatment at variable t_{dox} early in the culture protocol and then the gastruloids were further cultured to a final time (t_f) = 134 haa. Images represent at least five similar gastruloids measured at each time point. Scale bars, 200 µm. **b**, A–P axial patterns of Wnt-recorder labelling at different time points throughout gastruloid morphogenesis and a 6 h temporal resolution (n = 110 gastruloids; Supplementary Table 3). The lines and the shaded regions indicate the mean ± s.d., respectively, as a function of the A–P position x normalized to total gastruloid length l. Wnt activity first predicts a clear separation between anterior and posterior fates for t_{dox} = 96 haa (green curve). **c**, Wnt activity at 96 haa also predicts transcriptional cell fates. Cell types identified by Leiden clustering of single-cell transcriptomes at 120 haa (left). Relative composition of Leiden clusters according to Wnt activity recorded at t_{dox} = 96 haa (right). Wnt activity is broadly distributed throughout most clusters but excluded substantially from the somite, endoderm and endothelial clusters (see Methods). UMAP, uniform manifold approximation and projection; NMP, neuromesodermal progenitor; PSM, presomitic mesoderm.

96 haa additionally predict future transcriptional fates, we performed Wnt recording at 96 haa in gastruloids that also expressed our instantaneous Wnt reporter and then dissociated the GFP$^+$ (96 haa Wnt-high) and GFP$^-$ (96 haa Wnt-low) subpopulations at 120 haa for single-cell RNA sequencing (scRNAseq; Fig. 3a and Methods). The combined scRNAseq dataset from GFP$^+$ and GFP$^-$ cells revealed nine cell clusters (Fig. 3c(left)) corresponding to distinct cell types, using annotations from a recent scRNAseq atlas of mouse embryogenesis (Extended Data Fig. 4a)[25], and were largely consistent with previous gastruloid studies[26] (Fig. 3c and Extended Data Fig. 4b,c). Instantaneous Wnt activity at 120 haa was confined to the posterior-most neuromesodermal progenitor cluster (Extended Data Fig. 4d), consistent with our imaging data showing Wnt activity restricted to the elongating posterior domain (Extended Data Fig. 1d). In contrast, cells with recorded Wnt activity from 96 haa contributed to a broad range of fates but were excluded from three clusters: the anterior-most somite cluster[26] as well as the endoderm and endothelium clusters (Fig. 3c(right) and Extended Data Fig. 4e,f). These data confirm that early cell-to-cell differences in Wnt signalling at 96 haa (before Wnt posterior polarization) are already predictive of the future germ layer identity of cells (for example, endoderm versus mesoderm). Early signalling patterns thus provide information about both the future position and fate of cells.

Gastruloid polarization is driven by cell sorting

Our signal recording results suggested that Wnt-high and Wnt-low cells at 96 haa undergo subsequent cell rearrangements to transition from an unpolarized state to a single A–P axis. We next sought direct evidence of cell sorting using independent methods. We reasoned that in the strictest model of cell sorting—where cells can completely reorganize from any initial position—it should be possible to observe Wnt-dependent positional sorting even after gastruloids are dissociated into single cells and allowed to reaggregate. To test this prediction, we grew gastruloids expressing both our Wnt-recorder circuit and Wnt-transcriptional reporter, recorded Wnt activity from 90 to 96 haa to permanently label this signalling state and then enzymatically dissociated and reaggregated the labelled cells (Fig. 4a). Simulations confirmed that in a Turing model of polarization the recorded states before disaggregation would remain randomly distributed relative to the reformed A–P axis (Extended Data Fig. 5a,b). Conversely, a cell-sorting model predicts that cells that were Wnt-active and Wnt-inactive before dissociation would sort into distinct domains over time.

Our dissociation and reaggregation experiments revealed that by 114 haa (18 h after reaggregation) all gastruloids had reorganized based on the Wnt activity of cells at 96 haa (Fig. 4b). We observed cell-sorting polarization following two reaggregation protocols:

https://doi.org/10.1038/s41556-024-01521-9

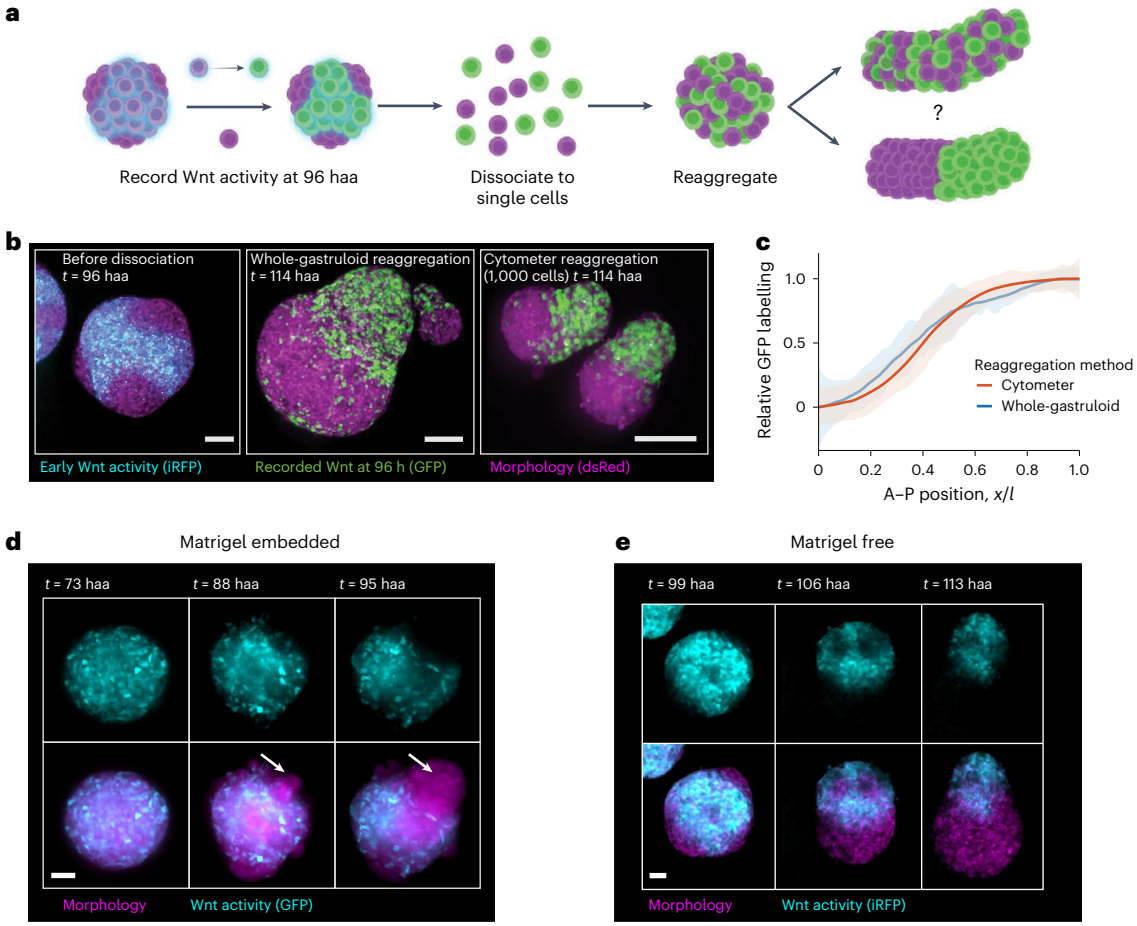

Fig. 4 | Gastruloid polarization is driven by cell sorting. a, Experimental design to test the polarization mechanism. Wnt activity is recorded in intact gastruloids at 96 haa, after which the samples are dissociated and reaggregated to test for reorganization of anteroposterior patterns. **b**, Representative images showing Wnt activity before dissociation (left) and the sorted positions of Wnt-recorded cells following reaggregation by either whole-gastruloid reaggregation (middle) or flow cytometer reaggregation (right; Methods). Images represent over 20 similar gastruloids from each condition. **c**, Relative distribution of GFP labelling along the A–P axis following reaggregation reveals anteroposterior sorting, with similar spatial profiles in both methods despite different aggregate sizes (Extended Data Fig. 5d and Supplementary Table 3; $n = 54$ gastruloids). The lines and the shaded regions indicate the mean ± s.d., respectively, as a function of A–P position. **d**, Still images from Supplementary Video 1 illustrating the dynamics of cellular rearrangements during the early stages of Wnt polarization. Images are representative of five similar gastruloids measured. The arrows point to gastruloids in which symmetry breaking was observed. **e**, Still images from Supplementary Video 3 illustrating the dynamics of cellular rearrangements during later stages of Wnt polarization. These rearrangements sort cells from patchy expression domains into a globally polarized signalling axis. Images are representative of two similar gastruloids measured. **b**,**d**,**e**, Maximum-intensity projections are shown. Scale bars, 100 µm (**b**) and 50 µm (**d**,**e**).

(1) reaggregation of an entire dissociated gastruloid in each well ('whole-gastruloid reaggregation') and (2) seed exactly 1,000 cells using a cell sorter to form each reaggregated gastruloid ('cytometer reaggregation'). Although all reaggregated samples showed polarization of Wnt-recorded cells, whole-gastruloid reaggregation produced a higher variability in gastruloid size and a higher frequency of multipolar gastruloids ($n = 28/48$) compared with cytometer reaggregation ($n = 0/34$), which suggests that cell sorting operates most efficiently on smaller domain sizes (Extended Data Fig. 5c). Although the monopolar gastruloids produced by the two reaggregation methods differed by about 2.6-fold in length (Extended Data Fig. 5d), they formed similar A–P profiles of Wnt-recorded cells (Fig. 4c). Cell sorting may contribute to recently reported scaling properties of gastruloids seeded from different initial numbers of cells[27].

We also confirmed cell sorting in unperturbed gastruloids by live imaging. We first imaged gastruloids expressing a Wnt transcriptional reporter ($P_{TCF/LEF}$–GFP–PEST) following CHIR washout at 72 haa to visualize the initial progression from homogenous to patchy Wnt activity and the initial emergence of axial polarity (Supplementary Videos 1 and 2). We embedded gastruloids in Matrigel to immobilize them during imaging[26,28]. In gastruloids where symmetry breaking could be observed (arrows in Fig. 4d and Supplementary Video 2), Wnt-active cells coalesced into clusters that merged and separated from the Wnt-inactive population. In addition, gastruloids that were not Matrigel-embedded were imaged from 96 to 108 haa to exclude potential differences due to embedding[6]. Despite substantial gastruloid movement during imaging, we observed rearrangement of Wnt-active cells to a single posterior domain (Fig. 4e and Supplementary Video 3). Particle image velocimetry of cell movements revealed that the posterior Wnt-active cells had higher motility than their anterior counterparts (Extended Data Fig. 5e–g and Supplementary Video 4). Together, our reaggregation and imaging studies indicate that a highly motile cell population rearranges within gastruloids from 96 to 108 haa to form a single posterior pole.

Wnt secretion is dispensable for axial polarization

We performed scRNAseq on 96 haa gastruloids expressing our instantaneous Wnt reporter (Fig. 5a) to further characterize the Wnt-high and Wnt-low subpopulations and generate hypotheses to explain their de-mixing. We observed two transcriptionally distinct clusters at 96 haa

https://doi.org/10.1038/s41556-024-01521-9

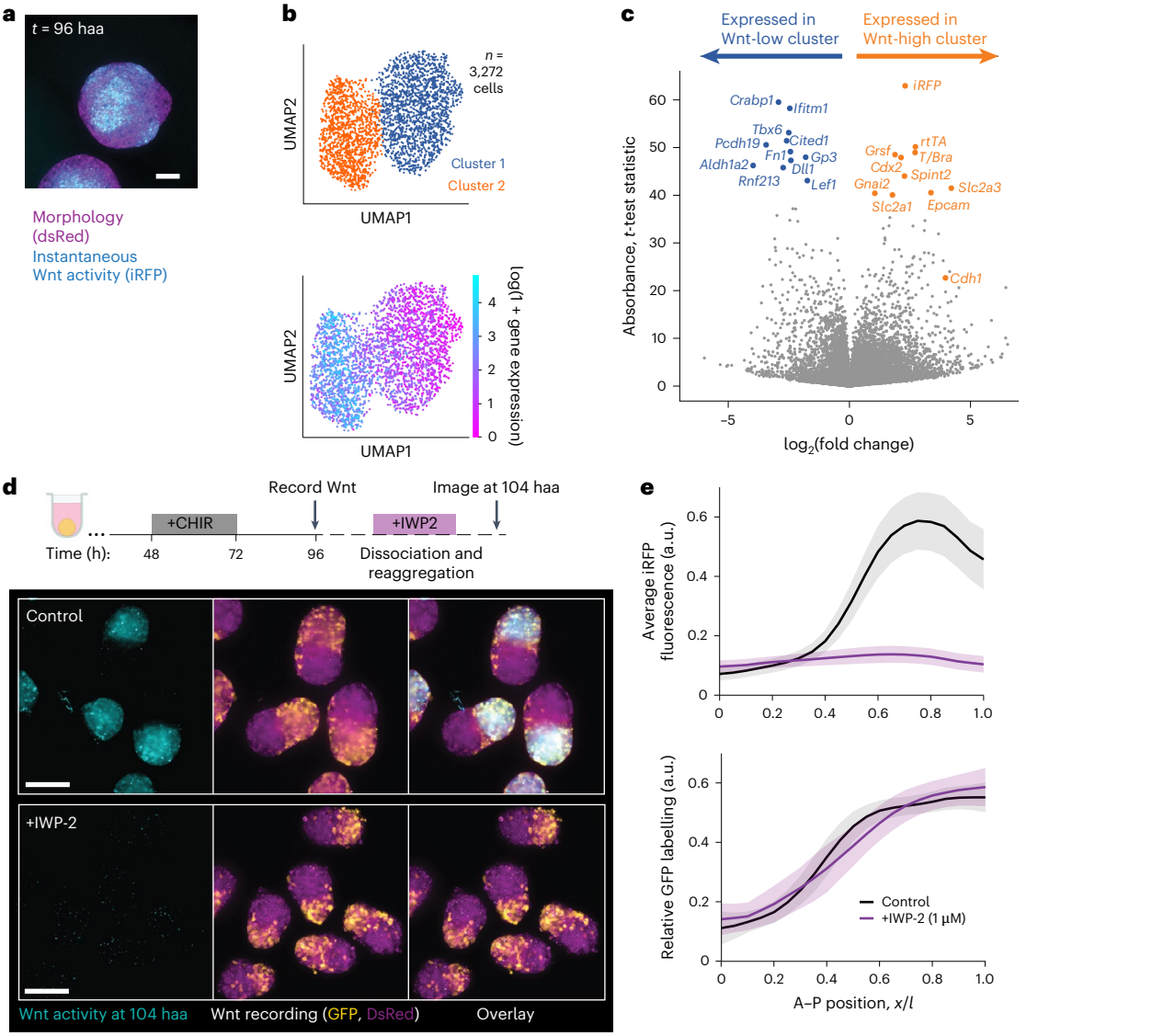

Fig. 5 | Sustained Wnt activity does not directly coordinate gastruloid cell sorting. a, Wnt activity at $t = 96$ haa is organized into 'patchy' patterns of local correlated domains lacking global polarization. Image is representative of 23 similar gastruloids measured. **b**, Single-cell RNAseq analysis of gastruloids collected at 96 haa. Leiden clustering identified two transcriptionally divergent cell types (top). Wnt activity (as measured by $P_{TCF/LEF}$-rtTA expression) was highly concentrated in cluster 2 ('Wnt active') and excluded from cluster 1 ('Wnt inactive'; bottom). **c**, Identification of genes that were differentially expressed between the two Leiden clusters. **d**, Representative images (bottom) from signal-recording and reaggregation experiments (top) performed in the presence of the Wnt secretion inhibitor IWP-2. Images are representative of >20 similar gastruloids measured in each condition. **a**,**d**, Maximum-intensity projections are shown. Scale bars, 100 µm. **e**, Average A–P profiles of final instantaneous Wnt activity (top) and the recorded Wnt activity before dissociation (bottom). Although IWP-2 eliminates the pattern of maintained Wnt activity, previous recordings of Wnt signalling continue to predict the final A–P cell positions. The lines and shaded regions indicate the mean ± s.d., respectively ($n = 49$ total gastruloids).

(Fig. 5b(top) and Extended Data Fig. 6a). Reads corresponding to the instantaneous Wnt reporter were confined to just one cluster, indicating that the Wnt signalling state marks the main transcriptionally distinguishable cell populations at this time point (Fig. 5b(bottom)).

We found that the expression levels of many genes beyond the Wnt-responsive synthetic genes (*iRFP* and *rtTA*) also differed between the two clusters (Fig. 5c). The Wnt-high cluster expressed the Wnt ligands *Wnt3a* and *Wnt5b* as well as BMP and FGF ligands (Extended Data Fig. 6b)[29]. Conversely, the Wnt-inactive population expressed a distinct set of signalling-associated genes including the Wnt inhibitor *FrzB* and the retinoic acid biosynthesis enzyme *Aldh1a2* (Extended Data Fig. 6b,c)[30]. The differential expression of Wnt ligands and Wnt inhibitors suggests that sustained Wnt signalling after CHIR removal might be maintained by autocrine signalling. To test for potential roles of continued Wnt ligand synthesis after CHIR washout, we treated 72 haa gastruloids with the Wnt secretion inhibitor IWP-2 (ref. 31), and monitored Wnt activity and morphogenesis. Treatment of 72 haa gastruloids with IWP-2 was sufficient to completely inhibit Wnt-reporter expression within 24 h (Extended Data Fig. 6d,e), which suggests that the Wnt-high subpopulation is indeed actively maintained by continued local Wnt secretion.

We next investigated whether the maintenance of distinct Wnt-high and Wnt-low subpopulations was necessary for cell sorting using our dissociation and reaggregation assay. Starting from our mESC line harbouring both the instantaneous Wnt-reporter and Wnt-recorder circuit, we recorded Wnt signalling states at 96 haa, dissociated gastruloids into single cells and reaggregated by cell sorting in the continued presence of IWP-2 (Fig. 5d). We observed that cell sorting was unaffected by the loss of Wnt signalling during reaggregation (Fig. 5d,e). These data suggest that Wnt-high and Wnt-low states are

actively maintained by continued secretion of Wnt ligands but that sustained Wnt signalling after 96 haa is dispensable for polarization. These results further argue against a Turing-like reaction-diffusion polarization mechanism involving Wnt activators and inhibitors.

Differential cadherin expression mediates cell sorting

What other differences in cell states might explain the partitioning of Wnt-high and Wnt-low cell subpopulations along an A–P axis? Our scRNAseq analysis also revealed prominent differences in expression of multiple cell adhesion-associated genes (Fig. 5c). Differential adhesion could provide a biophysical basis for cell sorting and gastruloid polarization: in the presence of cell migration to generate mixing, cells with matched combinations of adhesion receptors may phase-separate into distinct domains to minimize interfacial tension[32–34]. E-cadherin (also known as Cdh1), EpCAM and protocadherin 1 (Pcdh1) were all expressed in the Wnt-high cluster, whereas protocadherins 8 and 19 (Pcdh8 and Pcdh19, respectively) were primarily expressed in Wnt-low cells (Fig. 6a and Extended Data Fig. 7a). Not all adhesion receptors were differentially expressed; N-cadherin (also known as Cdh2) was expressed at similar levels in both clusters (Extended Data Fig. 7a).

We focused on Cdh1 and Pcdh19 due to their differential expression and previous reports of their roles in cell sorting[33,35]. We generated clonal mESC lines carrying dox-inducible GFP-tagged *Cdh1* and *Pcdh19* transgenes, which we termed iCdh1 and iPcdh19 cells, respectively (Fig. 6c and Extended Data Fig. 7b,c). We first measured how cadherin expression alters homotypic and heterotypic mechanical interactions using a spheroid fusion assay. We seeded 200 mESCs from a single cell line (wild-type, iCdh1 or iPcdh19 cells; in the presence or absence of dox) for 24 h to form a spheroid aggregate. We next incubated different pairs of spheroids together for 3 h to allow their association and fusion (Fig. 6d). By labelling the wild-type and cadherin-inducible cell lines with different fluorophores, we could measure the contact angle between aggregates to infer the relative interaction strength and interfacial tension (Methods). A wider contact angle indicates strong adhesion between spheroids, whereas a narrow contact angle indicates higher interfacial tension and a smaller contact area. We observed a dox-dependent decrease in the contact angle between pairs of wild-type and iPcdh19 spheroids as well as between iCdh1 and iPcdh19 spheroids compared with all homotypic and dox-uninduced pairs (Fig. 6e). Mouse ESCs are known to constitutively express Cdh1 (refs. 36,37), which potentially explains the stronger relative effect of inducible Pcdh19 expression.

We next tested whether cadherins are sufficient to mediate cell sorting in a single spheroid. We generated mosaic spheroids comprising equal mixtures of wild-type and either BFP-labelled iCdh1 or mCherry-labelled iPcdh19 cells, and measured the spatial distribution of each founder cell population after 24 h of aggregation (Fig. 6f and Methods). We observed dox-dependent radial sorting between mixtures of wild-type and iPcdh19 cells as well as between iCdh1 and iPcdh19 cells, with iPcdh19 cells positioned on the exterior and wild-type/iCdh1 cells in the interior (Fig. 6g,h and Extended Data Fig. 7d–f). Interestingly, we did not observe a transition from radial sorting to partitioning along a bipolar axis, which suggests that additional factors beyond differential expression of these cadherins may contribute to the final geometry of a gastruloid.

Finally, we tested whether perturbation of the patterns of cadherin expression during gastruloid development would alter anteroposterior polarization. We generated GFP-labelled wild-type and mCherry-labelled iPcdh19 gastruloids, fused pairs of gastruloids at 48 haa to generate a local domain of protocadherin-expressing cells and then imaged these at 93 haa (within the critical Wnt symmetry-breaking window; Fig. 6i,j). We quantified the morphology of the final fused gastruloids (Fig. 6k) as well as the direction of posterior Brachyury polarization[9,22] relative to the axis along which the spheroids were fused (Fig. 6l and Extended Data Fig. 7g,h). In all control conditions, the fused gastruloids had spherical morphologies (aspect ratio of approximately one) as well as random alignment between Brachyury polarization and fusion vectors. In contrast, fusion between dox-induced iPcdh19 and wild-type spheroids generated elongated morphologies (aspect ratio = 1.19 ± 0.14) as well as close alignment between the direction of Brachyury polarization and the iPcdh19 domain. These data thus suggest that a synthetic domain of Pcdh19 expression is sufficient to dictate the orientation of the body axis of a gastruloid and alter its morphogenesis.

Early Nodal–BMP signalling predicts the future position of a cell

What differences in the history of cells might lead them to adopt distinct Wnt-high and Wnt-low states at 96 haa? We hypothesised that heterogeneity in other signalling pathways involved in gastrulation (for example, Nodal and BMP signalling) could act as hidden variables that bias the future axial position of cells, potentially even before Wnt signalling is active (Fig. 7a)[1,38,39]. To characterize spontaneous activity in these pathways, we engineered clonal cell lines expressing either instantaneous Nodal (P_{AR8}–mCherry–PEST) or BMP (P_{IBRE4}–GFP–PEST) reporters. We observed spontaneous activity in both Nodal and BMP signalling pathways by 48 haa (Fig. 7b), a time point where Wnt activity was still uniformly low (Fig. 1d–f). Nodal–BMP activity was subsequently lost after CHIR stimulation, dropping to below the limit of detection by 96 haa (Extended Data Fig. 8a,b)—that is, by the time at which Wnt signalling breaks symmetry. Nodal activity at 48 haa increased in proportion to the seeding size of the gastruloid and was absent in cultured mESCs after 48 h in identical media, indicating a strong dependence on three-dimensional culture conditions (Extended Data Fig. 8c).

Fig. 6 | Differential cadherin expression mediates changes in tissue mechanics and cell sorting in stem cell aggregates and gastruloids. a, Illustration of cadherin-mediated cell sorting. Differential cadherin expression causes different cell–cell adhesion affinities, which in turn mediates multicellular phase separation in fluid tissues. **b**, Differential expression of cadherins—Cdh1 (top) and Pcdh19 (bottom)—between Wnt-high and Wnt-low gastruloid cells at 96 haa. Images (right) are representative of eight similar gastruloids measured for each stain. **c**, Schematic (top) and validation (bottom) of the iPcdh19 cell line. Images are representative of >5 similar cell clusters for each condition. **d**, Schematic of the contact angle assay to measure differential interfacial tension between mESC spheroids. **e**, Dox-dependent increases in interfacial tension were observed for aggregates of iPcdh19 spheroids with wild-type or iCdh1 spheroids ($n = 77$ constructs analysed). Data are the mean ± s.d. Statistical comparisons using a two-sided Student's *t*-test; $P = 5.1 \times 10^{-1}$, $P = 1.0 \times 10^{-2}$ and $P = 5.5 \times 10^{-6}$ (from left to right). **f**, Illustration of the mosaic spheroid assay to test the sufficiency of cadherin expression to drive cell sorting. Spheroids were aggregated from $n = 200$ cells comprising 100 cells each from two cell lines with different fluorescent labels. **g**, Representative images of mosaic spheroids after 24 h of aggregation. Medial slices are shown to highlight the radial structure. Images are representative of 17 and 25 spheroids measured with and without dox, respectively. **h**, Quantification of radial polarization as a measure of cell sorting revealed dox-dependent sorting of iPcdh19 cells from both wild-type and iCdh1 cells ($n = 153$ spheroids analysed). Statistical comparisons using a two-sided Student's *t*-test; $P = 8.8 \times 10^{-1}$, $P = 5.8 \times 10^{-2}$, $P = 2.2 \times 10^{-7}$ and $P = 7.4 \times 10^{-4}$ (from left to right). **i**, Protocol used to investigate the influence of iPcdh19 induction on gastruloid symmetry breaking. Clonal spheroids were aggregated for 48 h, fused, stimulated with CHIR from 48 to 72 haa and imaged at 93 haa. **j**, Representative images of fused wild-type (WT) and iPcdh19 gastruloids at 93 haa ($n = 58$ gastruloids; Supplementary Table 3). **b**,**c**,**d**,**j**, Maximum-intensity projections are shown. **b**,**c**,**d**,**g**,**j**, Scale bars, 50 µm (**b**,**d**,**g**,**j**) and 10 µm (**c**). **k**, The aspect ratio in gastruloids demonstrates dox-dependent elongation in wild-type + iPCdh19 fusion constructs. Statistical comparisons using a two-sided Student's *t*-test; $P = 6.6 \times 10^{-1}$ (left) and $P = 3.3 \times 10^{-4}$ (right). **l**, Dox-dependent alignment of the Brachyury polarization and fusion vectors in wild-type + iPCdh19 fusion constructs. $^{**}P \leq 0.01$, $^{***}P \leq 0.001$, $^{****}P \leq 0.0001$ and NS, not significant.

https://doi.org/10.1038/s41556-024-01521-9

To relate early Nodal–BMP signalling to the future A–P position of cells, we prepared Nodal-recorder and BMP-recorder gastruloids, recorded signalling activity at various times t_{dox} and imaged at 120 haa (Fig. 7c). These recordings revealed that Nodal–BMP signalling at 48 haa was already partially informative of the future A–P position of a cell (Fig. 7d and Extended Data Fig. 8d–i), with Nodal-recorded cells enriched in the anterior region and BMP-recorded cells enriched at the posterior. Remarkably, these opposing distributions suggest that gastruloids recapitulate the opposing Nodal–BMP patterning system found in vivo[38] despite lacking extra-embryonic tissues to pattern either signal. The Nodal and BMP recordings were less strongly polarized compared with our previous Wnt recordings (Fig. 3a), which

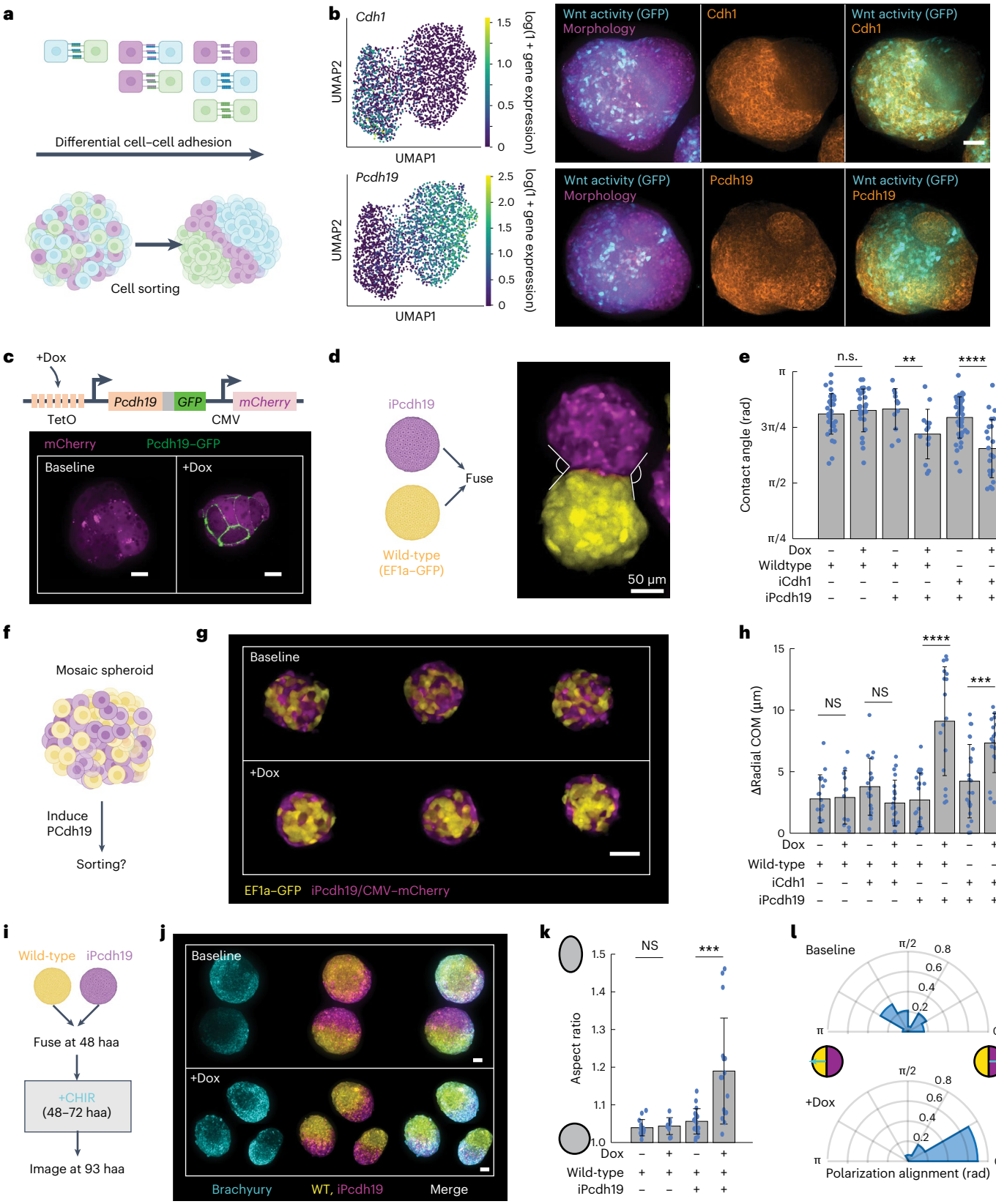

https://doi.org/10.1038/s41556-024-01521-9

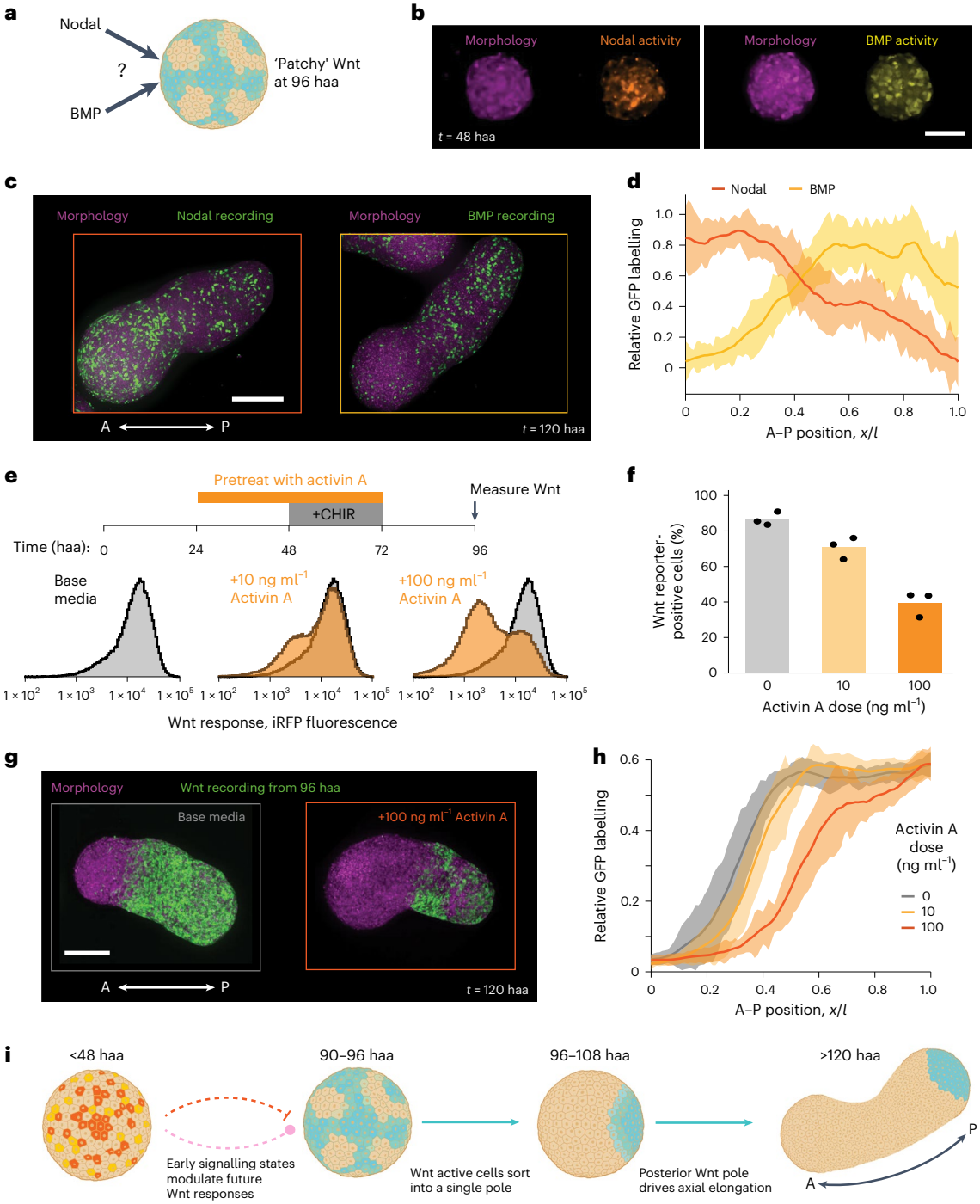

Fig. 7 | Early heterogeneity in TGFβ signalling modulates the duration of Wnt signalling to define anterior and posterior tissue domains. a, Illustration of our hypothesis. Heterogeneity in Wnt states at 96 haa may arise from earlier heterogeneity in other morphogen signalling pathways (Fig. 1a,b). **b**, Gastruloids show spontaneous signalling activity in both the Nodal (left) and BMP (right) pathways at $t = 48$ haa. Images are representative of seven similar Nodal reporter gastruloids and 11 similar BMP reporter gastruloids. **c**, Early Nodal and BMP activity was recorded immediately before the stimulation of Wnt activity with CHIR (3 h recording window, 45–48 haa; 200 ng ml^{-1} dox). Representative images of final distribution ($t_f = 120$ haa) of Nodal/BMP-recorded cells. Images are representative of ten Nodal-recorder gastruloids and 12 BMP reporter gastruloids. **d**, Quantification of the Nodal- and BMP-recorded cells in **c**. The lines and shaded regions indicate the mean ± s.d., respectively. **e**,**f**, Treatment with exogenous Activin A modulates the proportions Wnt 'on' and 'off' signalling states at 96 haa ($n = 3$ pooled biological replicates per condition, each replicate comprising at least 60 pooled gastruloids). **g**, Early Nodal activity alters gastruloid A–P proportions. Representative images of gastruloids in which Wnt activity was recorded at $t = 96$–97.5 haa and imaged at $t = 120$ haa, with and without Activin A pretreatment from 24 to 72 haa ($n = 42$ gastruloids total measured). **b**,**c**,**g**, Maximum-intensity projections are shown. Scale bars, 100 µm (**b**) and 200 µm (**c**,**g**). **h**, Quantification of Wnt-recording patterns demonstrates that Activin A pretreatment expands the Wnt-inactive anterior region ($n = 42$ gastruloids). The shaded regions indicate the s.d. as a function of the A–P position. See also Extended Data Fig. 10a,b. **i**, Illustration of the proposed model of gastruloid symmetry breaking. Early Nodal and BMP activity modulates the later response of cells to a uniform CHIR stimulus, yielding a heterogenous Wnt pattern. The heterogeneity then sorts to form a single pole of Wnt activity that defines the A–P axis and drives subsequent axial elongation.

suggests additional early asymmetries might also contribute to future anteroposterior fates.

We next investigated whether perturbation of early Nodal–BMP signalling affects subsequent gastruloid development. We first grew gastruloids expressing the instantaneous Wnt reporter, treated them with Activin A (a Nodal analogue) or BMP4 from 24 to 72 haa, and measured the Wnt-reporter activity by flow cytometry. All treatment conditions resulted in high uniform Wnt activity at 72 haa, demonstrating that pretreatment did not affect the initial response of cells to the CHIR stimulation (Extended Data Fig. 9a,b). Physiologically relevant doses of Activin A (10–100 ng ml^{-1}; Extended Data Figs. 8c and 9c,d) increased the proportion of Wnt-low cells at 96 haa, which suggests a causal relationship between early Nodal signalling and subsequent anterior fate (Fig. 7e,f). Even a brief 3 h pulse of 100 ng ml^{-1} Activin A at 48 haa was sufficient to reduce the duration of Wnt signalling at 96 haa, indicating that cells are highly sensitive to this stimulus (Extended Data Fig. 9e). BMP4 stimulation produced ambiguous effects, partially reducing the magnitude of Wnt signalling in all cells without producing bimodal Wnt-on and Wnt-off subpopulations (Extended Data Fig. 9b). Experiments in adherent mESC cultures revealed that BMP could either potentiate or inhibit Wnt activity in a complex dose- and time-dependent manner (Extended Data Fig. 9f), consistent with a recent report[40]. We chose to focus on Nodal signalling based on its consistent effects on Wnt signalling.

Next, gastruloids expressing the Wnt-recorder circuit were treated with Activin A from 24 to 72 haa and their final morphology was measured at 120 haa. Activin A pretreatment expanded the Wnt-low anterior domain at the expense of the Wnt-high posterior domain in a dose-dependent manner (Fig. 7g,h). The resulting gastruloids also exhibited altered morphology, with a shortened long axis and an expanded, denser anterior domain (Extended Data Fig. 10a,b). Conversely, complete inhibition of early Nodal signalling with the small molecule SB-431542 eliminated subsequent signalling and morphogenesis altogether, suggesting that activity through this pathway is necessary for gastruloid development (Extended Data Fig. 10c,d). Together, our data support a model in which early Nodal activity modulates later Wnt activity, gastruloid symmetry breaking and allocation of anterior and posterior domains.

Discussion

Our results reveal a mechanism through which biochemical and biophysical interactions between stem cells can spontaneously break symmetry to self-organize a body axis (Fig. 7i). Even in the absence of extrinsic cues, spontaneous Nodal and BMP signals create intrinsic heterogeneity within stem cell spheroids. This heterogeneity modulates how long cells maintain Wnt activity following uniform CHIR stimulation, resulting in patchy Wnt-high and Wnt-low domains at about 96 haa. Finally, cell migration and differential adhesion sort the patchy domains into a single Wnt-active pole. This pole breaks morphological symmetry in the gastruloid by defining a posterior organizer, which drives axial elongation[28,29].

Gastruloid polarization therefore emerges not from a canonical reaction-diffusion Turing instability but rather through a cell-sorting mechanism. Although the appearance of patchy Wnt activity patterns at 96 haa seems consistent with the intermediate state of a Turing pattern as it evolves to a single polarized pole, our signal-recorder circuits revealed that the future A–P positions of cells are already determined at this patchy stage (Fig. 3). Subsequent gastruloid reaggregation (Figs. 4 and 5), live imaging (Supplementary Videos 1–3) and cadherin induction experiments (Fig. 6) provided support for a model where cell sorting rearranges distinct cell populations to establish a global A–P axis. We emphasise that our results do not exclude all potential roles for reaction-diffusion patterning in gastruloid self-organization. For example, the patchy patterns of Wnt activity at 96 haa may reflect an earlier short-range Turing instability produced by self-sustained Wnt secretion.

Many molecular links in this model require further study. For example, we find that domains of distinct adhesion gene expression correspond to those with different Wnt signalling states. Wnt signalling may directly regulate this switch—for example, by downregulating the expression of Snai1, a repressor of Cdh1 and regulator of cell motility[28,41]. It is also possible that an upstream transcriptional programme leads to differences in both the duration of Wnt signalling and adhesion gene expression. Nodal and BMP themselves may only be two of several early asymmetries that influence the initial conditions of the axial coordinate system—for example, metabolic states[42] or radial tissue geometry[22] may also contribute to symmetry breaking. The complete network that links early cell states to future anteroposterior fates remains to be fully elucidated.

How does this self-organizing model of axial morphogenesis relate to the programme executed by the embryo? The polarized gastruloid is thought to model the primitive streak and tailbud, which represent just a part of the A–P axis of an embryo[43]. In vivo the posterior epiblast is prepatterned by gradients of signalling ligands supplied by extra-embryonic tissues[1,43]. Although the gastruloid engages the same Nodal, BMP and Wnt signalling pathways, their geometric organization is clearly different. The ability of the gastruloid to self-organize A–P patterns may reflect a developmental programme that reinforces graded patterning signals against errors and fluctuations[35,44]. The sequence of Nodal and Wnt signalling during gastruloid symmetry breaking might also be related to the temporal order of signalling events during primitive streak specification[45]. By differentially priming the responses of cells to uniform Wnt stimulation, Nodal can act as a temporal cue to generate spatial organization. Finally, it is also possible that gastruloid polarization represents a latent self-organizing programme of stem cells, which is not engaged during mouse development but rather reflects an evolutionary remnant from the first multicellular organisms[46]. The role of Wnt in patterning the primary body axis is highly conserved both in vertebrates[47] and in evolutionary divergent organisms such as flatworms[48], sea squirts[49] and hydra[50]. Gastruloid self-organization could reflect a programme first developed by the earliest multicellular organisms[50–52], which has since been elaborated upon by evolution.

By studying axial morphogenesis in a reduced model, we were able to isolate and define a mechanism of multicellular self-organization. The increasing complexity of stembryo models suggests that this is only one of the many self-organizing programmes that can emerge from aggregates of stem cells[53,54]. We anticipate that tracing signalling lineages will be a powerful and generalizable strategy to identify the intrinsic cues that drive these programmes. This strategy may benefit from next-generation signal recorders with improved bandwidth to record multiple morphogen signals in parallel or analogue information about signal magntitudes[55,56]. Defining the principles of biological self-organization will improve our understanding of multicellular symmetry breaking and may also uncover engineering routes towards disease modelling, regenerative medicine and biomanufacturing.

Online content

Any methods, additional references, Nature Portfolio reporting summaries, source data, extended data, supplementary information, acknowledgements, peer review information; details of author contributions and competing interests; and statements of data and code availability are available at https://doi.org/10.1038/s41556-024-01521-9.

References

1. Bardot, E. S. & Hadjantonakis, A.-K. Mouse gastrulation: coordination of tissue patterning, specification and diversification of cell fate. *Mech. Dev.* **163**, 103617 (2020).
2. Gregor, T., Wieschaus, E. F., McGregor, A. P., Bialek, W. & Tank, D. W. Stability and nuclear dynamics of the bicoid morphogen gradient. *Cell* **130**, 141–152 (2007).

3. Lord, N. D., Carte, A. N., Abitua, P. B. & Schier, A. F. The pattern of nodal morphogen signaling is shaped by co-receptor expression. *eLife* **10**, e54894 (2021).
4. Turner, D. A. et al. Anteroposterior polarity and elongation in the absence of extra-embryonic tissues and of spatially localised signalling in gastruloids: mammalian embryonic organoids. *Development* **144**, 3894–3906 (2017).
5. Beccari, L. et al. Multi-axial self-organization properties of mouse embryonic stem cells into gastruloids. *Nature* **562**, 272–276 (2018).
6. Veenvliet, J. V. et al. Mouse embryonic stem cells self-organize into trunk-like structures with neural tube and somites. *Science* **370**, eaba4937 (2020).
7. Miao, Y. et al. Reconstruction and deconstruction of human somitogenesis in vitro. *Nature* **614**, 500–508 (2023).
8. Ishihara, K. & Tanaka, E. M. Spontaneous symmetry breaking and pattern formation of organoids. *Curr. Opin. Syst. Biol.* **11**, 123–128 (2018).
9. van den Brink, S. C. et al. Symmetry breaking, germ layer specification and axial organisation in aggregates of mouse embryonic stem cells. *Development* **141**, 4231–4242 (2014).
10. Scoones, J. C., Banerjee, D. S. & Banerjee, S. Size-regulated symmetry breaking in reaction-diffusion models of developmental transitions. *Cells* **9**, 1646 (2020).
11. Sozen, B., Cornwall-Scoones, J. & Zernicka-Goetz, M. The dynamics of morphogenesis in stem cell-based embryology: novel insights for symmetry breaking. *Dev. Biol.* **474**, 82–90 (2021).
12. Simunovic, M. et al. A 3D model of a human epiblast reveals BMP4-driven symmetry breaking. *Nat. Cell Biol.* **21**, 900–910 (2019).
13. Sick, S., Reinker, S., Timmer, J. & Schlake, T. WNT and DKK determine hair follicle spacing through a reaction-diffusion mechanism. *Science* **314**, 1447–1450 (2006).
14. Raspopovic, J., Marcon, L., Russo, L. & Sharpe, J. Digit patterning is controlled by a Bmp–Sox9–Wnt Turing network modulated by morphogen gradients. *Science* **345**, 566–570 (2014).
15. Glover, J. D. et al. The developmental basis of fingerprint pattern formation and variation. *Cell* **186**, 940–956 (2023).
16. Hashmi, A. et al. Cell-state transitions and collective cell movement generate an endoderm-like region in gastruloids. *eLife* **11**, e59371 (2022).
17. Srivastava, V. et al. Configurational entropy is an intrinsic driver of tissue structural heterogeneity. Preprint at *bioRxiv* https://doi.org/10.1101/2023.07.01.546933 (2023).
18. Shyer, A. E. et al. Emergent cellular self-organization and mechanosensation initiate follicle pattern in the avian skin. *Science* **357**, 811–815 (2017).
19. Palmquist, K. H. et al. Reciprocal cell–ECM dynamics generate supracellular fluidity underlying spontaneous follicle patterning. *Cell* **185**, 1960–1973 (2022).
20. Kondo, S., Watanabe, M. & Miyazawa, S. Studies of Turing pattern formation in zebrafish skin. *Philos. Trans. R. Soc. A* **379**, 20200274 (2021).
21. Korinek, V. et al. Constitutive transcriptional activation by a β-catenin–Tcf complex in $APC^{-/-}$ colon carcinoma. *Science* **275**, 1784–1787 (1997).
22. Suppinger, S. et al. Multimodal characterization of murine gastruloid development. *Cell Stem Cell* https://doi.org/10.1016/j.stem.2023.04.018 (2023).
23. Serup, P. et al. Partial promoter substitutions generating transcriptional sentinels of diverse signaling pathways in embryonic stem cells and mice. *Dis. Model. Mech.* **5**, 956–966 (2012).
24. Morgani, S. M., Metzger, J. J., Nichols, J., Siggia, E. D. & Hadjantonakis, A.-K. Micropattern differentiation of mouse pluripotent stem cells recapitulates embryo regionalized cell fate patterning. *eLife* **7**, e32839 (2018).
25. Grosswendt, S. et al. Epigenetic regulator function through mouse gastrulation. *Nature* **584**, 102–108 (2020).
26. van den Brink, S. C. et al. Single-cell and spatial transcriptomics reveal somitogenesis in gastruloids. *Nature* **582**, 405–409 (2020).
27. Merle, M., Friedman, L., Chureau, C., Shoushtarizadeh, A. & Gregor, T. Precise and scalable self-organization in mammalian pseudo-embryos. *Nat. Struct. Mol. Biol.* **31**, 896–902 (2024).
28. Underhill, E. J. & Toettcher, J. E. Control of gastruloid patterning and morphogenesis by the Erk and Akt signaling pathways. *Development* **150**, dev201663 (2023).
29. Anand, G. M. et al. Controlling organoid symmetry breaking uncovers an excitable system underlying human axial elongation. *Cell* **186**, 497–512 (2023).
30. Chal, J. & Pourquié, O. Making muscle: skeletal myogenesis in vivo and in vitro. *Development* **144**, 2104–2122 (2017).
31. Wang, X. et al. The development of highly potent inhibitors for porcupine. *J. Med. Chem.* **56**, 2700–2704 (2013).
32. Steinberg, M. S. On the mechanism of tissue reconstruction by dissociated cells. I. Population kinetics, differential adhesiveness, and the absence of directed migration. *Proc. Natl Acad. Sci. USA* **48**, 1577–1582 (1962).
33. Toda, S., Blauch, L. R., Tang, S. K. Y., Morsut, L. & Lim, W. A. Programming self-organizing multicellular structures with synthetic cell–cell signaling. *Science* **361**, 156–162 (2018).
34. Stevens, A. J. et al. Programming multicellular assembly with synthetic cell adhesion molecules. *Nature* **614**, 144–152 (2023).
35. Tsai, T. Y.-C. et al. An adhesion code ensures robust pattern formation during tissue morphogenesis. *Science* **370**, 113–116 (2020).
36. Redmer, T. et al. E-cadherin is crucial for embryonic stem cell pluripotency and can replace OCT4 during somatic cell reprogramming. *EMBO Rep.* **12**, 720–726 (2011).
37. Soncin, F. et al. E-cadherin acts as a regulator of transcripts associated with a wide range of cellular processes in mouse embryonic stem cells. *PLoS ONE* **6**, e21463 (2011).
38. Xu, P.-F., Houssin, N., Ferri-Lagneau, K. F., Thisse, B. & Thisse, C. Construction of a vertebrate embryo from two opposing morphogen gradients. *Science* **344**, 87–89 (2014).
39. Massey, J. et al. Synergy with TGFβ ligands switches WNT pathway dynamics from transient to sustained during human pluripotent cell differentiation. *Proc. Natl Acad. Sci. USA* **116**, 4989–4998 (2019).
40. Camacho-Aguilar, E., Yoon, S., Ortiz-Salazar, M. A. & Warmflash, A. Combinatorial interpretation of BMP and WNT controls the decision between primitive streak and extraembryonic fates. *Cell Syst.* **15**, 445–461 (2024).
41. Mayran, A. et al. Cadherins modulate the self-organizing potential of gastruloids. Preprint at *bioRxiv* https://doi.org/10.1101/2023.11.22.568291 (2023).
42. Dingare, C., Cao, D., Yang, J. J., Sozen, B. & Steventon, B. Mannose controls mesoderm specification and symmetry breaking in mouse gastruloids. *Dev. Cell* **59**, 1523–1537 (2024).
43. Arias, A. M., Marikawa, Y. & Moris, N. Gastruloids: pluripotent stem cell models of mammalian gastrulation and embryo engineering. *Dev. Biol.* **488**, 35–46 (2022).
44. Pinheiro, D., Kardos, R., Hannezo, É. & Heisenberg, C.-P. Morphogen gradient orchestrates pattern-preserving tissue morphogenesis via motility-driven unjamming. *Nat. Phys.* **18**, 1482–1493 (2022).
45. Schüle, K. M. et al. Eomes restricts Brachyury functions at the onset of mouse gastrulation. *Dev. Cell* **58**, 1627–1642 (2023).

46. Anlas, K. & Trivedi, V. Studying evolution of the primary body axis in vivo and in vitro. *eLife* **10**, e69066 (2021).
47. Petersen, C. P. & Reddien, P. W. Wnt signaling and the polarity of the primary body axis. *Cell* **139**, 1056–1068 (2009).
48. Petersen, C. P. & Reddien, P. W. Polarized notum activation at wounds inhibits Wnt function to promote planarian head regeneration. *Science* **332**, 852–855 (2011).
49. Feinberg, S., Roure, A., Piron, J. & Darras, S. Antero–posterior ectoderm patterning by canonical Wnt signaling during ascidian development. *PLoS Genet.* **15**, e1008054 (2019).
50. Wang, R., Steele, R. E. & Collins, E.-M. S. Wnt signaling determines body axis polarity in regenerating *Hydra* tissue fragments. *Dev. Biol.* **467**, 88–94 (2020).
51. Lovas, J. R. & Yuste, R. Dissociation and reaggregation of *Hydra vulgaris* for studies of self-organization. *STAR Protoc.* **3**, 101504 (2022).
52. Ferenc, J. et al. Mechanical oscillations orchestrate axial patterning through Wnt activation in *Hydra*. *Sci. Adv.* **7**, eabj6897 (2021).
53. Amadei, G. et al. Embryo model completes gastrulation to neurulation and organogenesis. *Nature* **610**, 143–153 (2022).
54. Tarazi, S. et al. Post-gastrulation synthetic embryos generated ex utero from mouse naive ESCs. *Cell* **185**, 3290–3306 (2022).
55. Bhattarai-Kline, S. et al. Recording gene expression order in DNA by CRISPR addition of retron barcodes. *Nature* **608**, 217–225 (2022).
56. Choi, J. et al. A time-resolved, multi-symbol molecular recorder via sequential genome editing. *Nature* **608**, 98–107 (2022).

Methods

Plasmids and cloning

Linear DNA fragments were amplified via PCR using CloneAmp HiFi PCR premix (Takara Bio, 639298). The PCR products were cut from agarose gels and purified using a Nucleospin gel purification kit (Takara Bio, 240609). Plasmids (Supplementary Table 1) were assembled from linear fragments using In-Fusion HD (Takara Bio, 638910) and amplified in Stellar chemically competent *Escherichia coli* (Takara Bio, 636763) via ampicillin-resistant selection. The plasmid DNA was extracted using a miniprep kit (Qiagen, 27104). All plasmid verification was performed by Sanger (Azenta) or nanopore (Plasmidsaurus) sequencing.

Expression vectors were cloned into a piggyBac vector plasmid containing 5′ and 3′ flanking repeats to facilitate PBase insertion[28]. Plasmids encoding Cre recombinase, the 'stoplight' recording locus and the Wnt-sensitive TOPFlash enhancer ($P_{TCF/LEF}$) were purchased from Addgene (catalogue numbers 89573, 62732 and 12456, respectively). Sentinel enhancers responding to transcriptional output from Activin/Nodal (P_{AR8}) and BMP (P_{IBRE4}) were subcloned from AR8-Cerulean and IBRE4-Cerulean constructs (a gift from K. Zaret). Plasmids generally contained a constitutively expressed fluorescent protein to serve as a selection marker during cell line generation.

Cell culture

All reported experiments were performed using cell lines derived from E14tg2a mESC cells (ATCC CRL-1821, purchased for this study). The E14tg2a cells were first thawed and plated on mitotically inactivated feeder cells (Millipore Sigma, PMEF-DR4-M) in basal growth medium comprising GMEM (Millipore Sigma, G6148) supplemented with 10% ESC-qualified fetal bovine serum (R&D Systems, S10250), 1×GlutaMAX (Gibco, 35050-061), 1×MEM non-essential amino acids (Gibco, 11140-470050), 1 mM sodium pyruvate (Gibco, 11360-070), 100 µM 2-mercaptoethanol (Gibco, 47121985-023) and 100 units ml^{-1} penicillin–streptomycin (Gibco, 15140-122). After reconstitution, the E14tg2a cells were trypsinized and passaged onto a 25 cm^2 tissue culture flask coated with 0.1% gelatin and cultured in 2i + LIF medium comprising basal growth medium further supplemented with 1,000 units ml^{-1} LIF (Millipore Sigma, ESG1107), 2 µM PD0325901 (Tocris, 4192) and 3 µM CHIR (Tocris, 4423).

Propagation of cell lines was thereafter performed in 2i + LIF medium on gelatin-coated tissue culture plastic unless otherwise noted. Cells were maintained at 20–75% confluency. Passaging was performed by aspirating the remaining growth medium, washing in PBS (Gibco, 14190144) and trypsinizing for 5 min at 37 °C (TrypLE Express, Gibco, 12605028). The trypsin was quenched with 2i + LIF medium and the cells were then pelleted by centrifugation at 135*g* for 5 min. Residual trypsin and medium were then aspirated and replaced with fresh medium before replating in a fresh tissue culture vessel. The passage ratios varied from 1:5 to 1:10.

Cell line generation

Engineered mESC lines (Supplementary Table 2) were generated using the piggyBac random integration system. A chassis cell line was first cultured to low-to-mid confluency (30–50%) in a 35 mm dish in 2i + LIF medium. Transfection mixtures were prepared in 250 µl Gibco Opti-MEM (Fisher Scientific, 31-985-070) containing 5 µl Lipofectamine STEM transfection reagent (Thermo Fisher, STEM00001), 2,080 ng vector plasmid and 420 ng PBase 'helper' plasmid (System Biosciences). After preparation, the transfection mixtures were equilibrated at room temperature for 30 min. The chassis cell cultures were given fresh 2i + LIF medium immediately preceding transfection. The transfection mixture was then added dropwise to the chassis cells and gently mixed via rocking.

Cultures were propagated for at least four days following transfection, by which vector expression is predominantly driven by genomically integrated constructs. The cells were then trypsinized into a single-cell suspension for fluorescence-activated cell sorting using a Sony SH800 sorter. Cytometry events were first sorted for single cells based on scattering profiles; transformed cells were then identified via fluorescence signals. Candidate clonal cultures were generated by sorting single cells into separate wells of a 96-well plate. The colonies were left unperturbed for 7–10 days following sorting, after which they were assessed via microscopy to identify promising candidates via fluorescence intensity and colony morphology (that is, preference for round colonies with smooth boundaries). Candidate clonal colonies were then identified and supplemented with an additional 150 µl 2i + LIF medium and fed every other day until 14 days post seeding. At 14 days, the promising clones were trypsinized and passaged onto a 12-well plate. Lines that remained viable were then further expanded and functionally assessed. The lines were tested and confirmed to be negative for mycoplasma (ATCC universal mycoplasma kit, 30-1012K).

Statistics and reproducibility

A small proportion of gastruloids (<10%) failed to elongate (consistent with field standards for gastruloid reproducibility[4]) and were excluded from the A–P profile analyses (Figs. 3b, 7d–g and Extended Data Fig. 8d,e). For the whole-gastruloid reaggregation experiments (Fig. 4c and Extended Data Fig. 5c), very small satellite ESC cell aggregates as well as multipolar aggregates were excluded as described below. Fractions of multipolar aggregates were quantified in Extended Data Fig. 5c. Our statistical analyses assumed our measurements were normally distributed but this was not formally tested. No statistical methods were used to pre-determine sample sizes; sample sizes (Supplementary Table 3) were designed to be similar to those reported in recent publications[5,27].

Signal-recording benchmarking

Signal-recording cell lines were benchmarked in adherent cultures cultured on gelatin-coated tissue culture plastic. We sorted at least ten candidate clones for each recording circuit architecture and screened each clone for a combination of low leakiness (in signalling-low conditions) and high labelling efficiency (in signalling-high conditions); the best-performing clone of each design was selected for further characterization. Minimum recording window measurements (Fig. 2c, right column) and dox concentration calibration (Extended Data Fig. 2a) were performed in steady-state 2i + LIF media. All other signal-recording calibration measurements were performed in N2B27 basal media, supplemented with dox, CHIR or recombinant morphogen proteins according to the experimental condition (Fig. 2c(left column),d,e and Extended Data Figs. 2b–d, 10c). The media were exchanged with fresh N2B27 at least 24 h before the recording experiments to allow cells to equilibrate to basal media conditions. For Wnt-recorder fidelity testing (Fig. 2c), Wnt dose response (Extended Data Fig. 2b) and morphogen crosstalk experiments (Fig. 2e and Extended Data Fig. 2c), morphogen signals were added to media simultaneously with the onset of the dox recording window and then washed out following cessation of the dox recording window. Cells were expanded for at least 24 h following cessation of dox treatment and then assayed via flow cytometry.

Gastruloid protocol

Gastruloids were grown in N2B27 medium comprising a 1:1 mixture of DMEM/F-12 (Gibco, 11320033) and neurobasal (Gibco, 21103049) media supplemented with 100 µM 2-mercaptoethanol, 1:100 N-2 (Gibco, 17502048), 1:50 B-27 (Gibco, 17504044) and 100 units ml^{-1} penicillin–streptomycin (Gibco, 15140-122). Seed cultures were maintained in 2i + LIF medium previous to gastruloid formation to minimize pre-existing heterogeneity in early stage gastruloids, which may bias symmetry breaking. For 'LIF only' preculture gastruloids, cells were transferred from 2i LIF medium to medium without either PD0325901 or CHIR for six days (two passages) before gastruloid formation.

To form gastruloids, seed cultures were trypsinized, pelleted and then washed twice with PBS (separated by additional 5 min centrifugations at 135*g*) to remove residual CHIR. Following the second PBS wash, the cells were resuspended in N2B27 medium and transferred to a cell sorter for fluorescence-activated cell sorting. Sorting events were gated for single cells based on the scattering profiles. For signal-recording gastruloids, cells were further gated against GFP expression to avoid contamination from the small fraction of cells (about 0.1%) that had already excised dsRed. To form gastruloids, 200 individual cells were sorted into each of the 60 central wells of a 96-well round-bottomed ultra-low-attachment microplate (Corning, 7007). The central wells were pre-filled with 40 µl N2B27 to receive cells. To minimize the effects of evaporation at the edges of the plate, the perimeter wells were filled with 150 µl PBS supplemented with 1,000 units ml^{-1} penicillin–streptomycin.

Following seeding, the gastruloids were transferred to a cell culture incubator and left unperturbed for 48 h unless otherwise noted. At $t = 48$ h, the gastruloids were fed 150 µl N2B27 medium further supplemented with 3 µM CHIR to stimulate Wnt activity. At $t = 72$ h, 150 µl CHIR-containing medium was removed from the gastruloid wells and the gastruloids were fed 150 µl fresh N2B27 medium without CHIR. A similar feeding (150 µl medium removed and 150 µl fresh N2B27 added) was performed every 24 h for the remaining period of gastruloid morphogenesis. Signal recording during gastruloid morphogenesis was performed via the transient addition of 150 µl medium supplemented with 100 ng ml^{-1} dox. Recording windows were either 90 min (for Wnt recording) or 3 h (for BMP and Nodal). The dox was washed out with two successive 150 µl media changes, leading to a total dilution of approximately 1:20 (sufficient to bring the dox concentration below the recording threshold defined in Extended Data Fig. 2a).

Gastruloids were assayed either by imaging or by flow cytometry. To prepare samples for imaging, the gastruloids were fixed in 4% paraformaldehyde for 2 h at 4 °C on a nutator. The samples were then washed twice in PBS to remove the paraformaldehyde and either transferred for immunofluorescence labelling or immediately transferred to a glass-bottomed 96-well plate for imaging. To assess gastruloids via flow cytometry, a minimum of $n = 30$ gastruloids were first pooled into a 1.5 ml Eppendorf tube, centrifuged (500*g* for 3 min), washed in PBS and then trypsinized in 100 µl TrypLE Express at 37 °C. The gastruloids were trypsinized for 3 min, retrieved and triturated to dislodge them, and returned to 37 °C for an additional 3 min to complete digestion. Trypsinization was then quenched with 300 µl N2B27, after which the samples were immediately assayed via flow cytometry. Cytometer events were first gated for events corresponding to cells based on the forward and back scatter profiles, and then for single cells based on the height and area of the forward scatter events (Extended Data Fig. 1e). For analysis of Wnt-active and -inactive cell populations, a threshold that separated the Wnt-inactive (measured at 48 haa) and Wnt-active (measured at 72 haa) states was defined (Extended Data Fig. 1f).

Immunofluorescence

Gastruloid staining was performed according to previously reported protocols[17]. Briefly, cohorts of paraformaldehyde-fixed gastruloids were pooled into single wells of ultra-low-attachment 96-well plates and washed twice with PBS to remove any residual PBS. All buffer exchanges were performed under a dissection microscope to maximize buffer turnover while minimizing sample loss due to accidental aspiration. Gastruloids were permeabilized overnight at 4 °C with nutation in PBSFT buffer (89.8% PBS, 10% fetal bovine serum and 0.2% Triton X-100). The PBSFT was then removed and exchanged for PBSFT containing dilutions of primary antibodies to the targets of interest. The following primary dilutions were used: 1:200 for rabbit anti-Pcdh19 (Abcam, ab191198), 1:100 for rabbit anti-Aldh1a2 (Abcam, ab156019), 10 µg ml^{-1} goat anti-Brachyury (R&D Systems, AF2085) and 1:200 for rabbit anti-Cdh1 (Cell Signaling Technology, 3195T). Primary antibody incubation was performed overnight at 4 °C with nutation. Following the primary incubations, the samples were treated with PBSFT for three consecutive washes. A further two sets of three serial wash sequences, with 1 h of nutation between each wash sequence, were performed resulting in a total of nine washes. The samples were then incubated overnight, at 4 °C with nutation, with fluorescently conjugated secondary antibodies (goat anti-rabbit Alexa Fluor 647 conjugate; Invitrogen, A27040) diluted 1:500 in PBSFT. Following the secondary antibody incubation, the samples were washed a further nine times following the same protocol described earlier. The samples were then transferred to a glass-bottomed 96-well plate for imaging (Cellvis, P96-1.5H-N).

Image processing and quantification

All imaging data reported were acquired on a Nikon Eclipse Ti confocal microscope with a 600 Prior linear motorized stage, a Yokogawa CSU-X1 spinning disk, an Agilent laser line module 601 containing 405, 488, 561 and 650 nm lasers, and an iXon DU897 EMCCD camera. Images were acquired as three-dimensional hyperstacks using the NIS Elements version 4.40.00 software (Nikon, Inc) and converted to maximum-intensity projections using the ImageJ version 1.54j software. For low-signal regimes ($P_{TCF/LEF}$–GFP live imaging and late-stage gastruloid $P_{TCF/LEF}$–iRFP patterns), median filtering was performed (kernel of 2–5 pixels) to denoise and improve the contrast. Near-infrared images were further background-subtracted to correct for a heterogeneous background field using a sample-free background image.

Quantification was performed using custom software in MATLAB version R2024a. Briefly, maximum-intensity projections were normalized on a [0,1] interval by first subtracting the background fluorescence and then dividing by the 99th percentile pixel value, each on a channel-by-channel basis. For sparse images (for example, sparse GFP labelling), the maximum pixel percentile was increased to avoid overamplification. Gastruloid segmentation was performed on a morphological image generated by adding the 488 nm and 561 nm excitation channel images (to account for total recorder locus signal). Morphological images were binarized, manually trimmed to separate neighbouring gastruloids from co-segmenting, and then dilated, eroded and filled to smoothen boundaries. Individual gastruloids were linearized by first skeletonizing with the MATLAB bwskel() function (MinBranchLength = 200). The resultant A–P axis trace was clipped if necessary (to avoid over-fitting on boundary artifacts) and manually extended to the anterior and posterior poles to create a curvilinear axis. The posterior pole of the axis was manually identified based on gastruloid morphology and/or Wnt signalling activity and the curvilinear axis was assigned units of distance based on geodesic distance from the anterior pole computed by bwdistgeodesic(). Pixels contained within a gastruloid segment were assigned an axial coordinate based on the geodesic distance of the closest curvilinear axis point and then binned over intervals of dL = 10 µm. One-dimensional fluorescence profiles were computed by averaging values within all gastruloid pixels corresponding to a single axial distance bin. A small proportion (<10%) of gastruloid samples that failed to elongate were excluded from analysis (due to lack of a clear anteroposterior axis).

For Wnt-recording quantification, fractional labelling profiles are reported as the ratio of the average normalized GFP fluorescence to the sum of the average normalized GFP and average normalized dsRed fluorescence. To average profiles over experimental replicates, profiles were rescaled onto a unit A–P axis $x/l = [0,1]$. For each experimental condition, the mean, s.d. and s.e.m. values were computed for each axial position. To compute the integrated Wnt signalling activity

$$I(x) = \int_{t_0}^{t_f} W(x, t')\, dt'$$

(Extended Data Fig. 3f), fractional labelling profiles $W(x,t)$ were first individually normalized to the unit integral over the A–P axis and

then added from t_{dox} = 96 h to t_{dox} = 120 h. An additional profile from t_f = 134 h was extracted from the final $P_{TCF/LEF}$–iRFP fluorescence and similarly normalized to the unit integral along the A–P axis, and then added to the total integral $I(x)$ to capture the final signalling profile.

Spatial profiles of Wnt signalling in early gastruloids (Fig. 1d and Extended Data Fig. 1d) were quantified to assess relative heterogeneity and polarization (Fig. 1g and Extended Data Fig. 1g). Gastruloids were first normalized and segmented as described above. Images were then further denoised using a median filter (14 µm × 14 µm kernel) to remove high spatial frequency noise. Relative heterogeneity was determined by computing the s.d. of the pixel intensities within a segmented gastruloid area. Relative polarization was computed according to

$$P = \frac{\mathrm{COM}_{\mathrm{Wnt}} - \mathrm{COM}_{\mathrm{morph}}}{r_a}$$

where $\mathrm{COM}_{\mathrm{morph}}$ is the morphological centre of mass (determined by EF1a–dsRed fluorescence), $\mathrm{COM}_{\mathrm{Wnt}}$ is the centre of mass of the Wnt activity pattern and r_a is the morphological semimajor axis length. For calculation of radial polarization in cadherin-induced spheroids (Fig. 6h), gastruloids were segmented and binned based on distance from the morphological centre of mass and then averaged to generate radial profiles of average fluorescence within channels. Radial profiles were then converted to radial centres of mass and the differences between channels were computed to assess radial polarization.

Morphological analysis of fused gastruloids was performed using custom software in MATLAB. For surface tension measurements, contact angles were manually annotated and then averaged and compared between conditions according to a two-sample Student's *t*-test (Fig. 6d,e). To measure morphological elongation in fused gastruloids following CHIR stimulation (Fig. 6k), aspect ratios were calculated as the ratio of the major-to-minor axis lengths. Polarization alignment (Fig. 6l) was calculated by first computing the fusion vector (defined as the vector between the centres of mass of mCherry and GFP cell labels), then computing the polarization vector (defined as the vector between the centre of mass of Brachyury staining and the morphological centre of mass) and finally computing the angle between those vectors. A convention was chosen such that an angle of zero corresponds to alignment of Brachyury and mCherry, and an angle of π corresponds to alignment of Brachyury and GFP.

Live imaging

Gastruloids were immobilized for live imaging via Matrigel embedding (Supplementary Videos 1, 2 and 4). To prepare Matrigel matrix (Corning, catalogue number 356231), frozen aliquots were thawed overnight at 4 °C. Glass-bottomed 35 mm dishes (Cellvis, D35-20-1.5-N) and pipette tips were chilled to temperature in a controlled cold room at 4 °C and the central imaging well was coated with Matrigel reagent. The Matrigel-coated dish was then transferred to a metal surface on ice to prevent gelling. Gastruloids were collected and dispersed into cooled Matrigel while maintaining minimal media carryover (roughly 10 µl volume). Approximately 6–12 gastruloids were embedded per experiment. The gastruloids were manually separated via pipette manipulation to ensure even spacing and transferred to 37 °C for 10 min to solidify the Matrigel matrix. Prewarmed N2B27 medium (2 ml) was then added to the glass-bottomed dish and the samples were transferred to a microscope-mounted environmental chamber (Okolab) to maintain appropriate temperature, humidity and CO_2 during imaging. The samples were imaged using a Nikon Eclipse Ti confocal microscope. Videos were collected over 24–30 h, with frames acquired once every 10 min. Individual frames were acquired at four *z*-planes. Images were median filtered to denoise and maximum-intensity projected to generate the final videos.

To measure cell motivity (Extended Data Fig. 5e–g), particle image velocimetry analysis was performed on gastruloids expressing a nuclear marker (H2B–iRFP) using the MATLAB PIVlab graphical user interface[57]. Briefly, H2B–iRFP videos were collected at 10 min intervals, median filtered and thresholded to remove background noise, after which velocity vectors were computed using nesting windows of 128, 64 and 32 pixels. Next, the resulting vector maps were segmented to remove vectors outside the gastruloid region and converted into directionless motility magnitudes by taking the Euclidean norm of each vector. Average motility maps were computed by averaging over the last 21 frames of the video (that is, over 3.5 h of collection) and converted to A–P profiles by averaging as described previously.

scRNAseq

To prepare gastruloids for single-cell sequencing, samples were first pooled into a 1.5 ml Eppendorf tube. At least 50 gastruloids were pooled for each experimental condition. Following pooling, the gastruloids were centrifuged (500*g* for 3 min), washed in PBS, centrifuged once more (500*g* for 3 min), resuspended in 100 µl trypsin and transferred to 37 °C. After 3 min, the gastruloid–trypsin mixture was retrieved, triturated to dislodge gastruloids and returned to 37 °C for an additional 3 min. The samples were then quenched with 300 µl N2B27 medium and immediately transferred to a cell sorter (Sony SH800). For 96 h gastruloids, cytometer events corresponding to single cells were identified based on light scattering profiles and then recovered into 500 µl N2B27 medium. For 120 h gastruloids, single-cell events were further gated based on GFP fluorescence and recovered into two separate recovery tubes (each containing 500 µl N2B27 medium). The recovered cells were immediately centrifuged (500*g* for 5 min) and resuspended in 50 µl PBS. A 10 µl fraction was stained for dead cells with trypan blue and automatically counted (Invitrogen Countess) to assess the density and viability of the recovered cells. The samples were then diluted to a target cell density of 1,000 cells μl^{-1}. Both 96 and 120 h samples maintained over 80% cell viability by this step.

Following dilution in PBS, the cells were kept on ice and transferred to a Chromium Controller (10x Genomics) to generate gel-in-bead emulsions for single-cell RNA labelling. Microfluidic chip lanes (Chip K, 10x Genomics) were loaded to a target recovery of 5,000 cells per lane. We used a Single cell 5′ v2 reagent kit (10x Genomics) to enable optional direct capture of non-polyadenylated messenger RNA from synthetic reporter genes. Following gel-in-bead emulsion formation, the reverse transcription reaction was performed with master mix supplemented with the following direct capture primer targeting iRFP (5 pmol per sample lane): 5′-AAGCAGTGGTATCAACGCAGAGTACCTCTTCCATCACGCCGATCTG-3′.

Gene expression libraries were then generated from sample complimentary DNA according to the manufacturer's protocol. Briefly, cDNA samples were fragmented and selected for a target size via double-sized magnetic bead selection (Beckman-Coulter SPRIselect). Next, the samples were ligated with adaptor oligonucleotides and PCR-amplified with dual library indices for sample demultiplexing. The library concentrations were assessed by fluorometry (Qubit) and the size distribution was measured with automated electrophoresis (Agilent Bioanalyzer). Samples were pooled to target equal concentration and submitted for pooled sequencing on an Illumina NovaSeq SP 100 nt Flowcell v1.5 system. The library was sequenced to a depth of 47,000 reads per cell.

Analysis of scRNAseq data

Raw FastQ files were demultiplexed by W. Wang at the Princeton Genomics Core Facility. The mm10_2020 transcriptome was modified to include BFP, iCre, iRFP, rTTA and the 'Stoplight Recorder' as additional elements for alignment in the analysis pipeline, as per 10x documentation (the FASTA files for these gene products are available at GitHub; https://github.com/toettchlab/McNamara2024). Demultiplexed files were then individually converted to count tables using the

10x CellRanger 6.0.1 pipeline per outlined documentation. All jobs were submitted through the Princeton LSI gencomp2 computing cluster.

Single-cell mRNA count matrices were analysed with the Single cell analysis in Python (Scanpy) toolkit. For 120 h datasets, GFP^+ and GFP^- libraries were conjoined into a single dataframe retaining conditional labels. Initial filtering was performed to exclude genes detected in fewer than three cells as well as cells with either fewer than 500 genes or fewer than 3,000 total assigned reads. Secondary filtering was performed to exclude cells with either more than 8% counts corresponding to mitochondrial genes or more than 30% counts corresponding to ribosomal RNA. Counts were then normalized to 10,000 counts per cell, log-transformed and regressed to remove variation contributed by cell cycle-associated genes. Highly variable genes were normalized to zero mean and unit variance, batch corrected and decomposed via principal component analysis. A nearest-neighbour graph was computed on the top 40 principal components using a 20-member local neighbourhood and visualized by uniform manifold approximation and projection. Cell types were identified by Leiden clustering (resolution = 0.4 for 96 h data; resolution = 0.6 for 120 h data).

Leiden clusters were associated with previously annotated reference cell types by comparing marker genes that were differentially expressed between both datasets. The mean log-transformed expression of genes within each cluster was compared to the overall mean using a Student's *t*-test. Candidate marker genes for each cluster were ranked according to test statistics, filtered for $P < 0.01$ and up to 50 top ranked genes were retained as marker genes for each Leiden cluster. Marker genes were then compared with a reference atlas[32] comprising 30 marker genes for previously annotated embryonic cell types to determine overlap of shared markers between Leiden clusters and reference atlas cell types. The statistical likelihoods of observed overlaps were computed by comparing overlap degrees to the binomial probability of drawing the same number of common genes from a random list of all unique atlas marker genes.

Signal-recording fractions within Leiden clusters were calculated by comparing the relative distributions of cell types across recording conditions. For each cluster k, we calculated the conditional probability that a cell would occupy cluster k given its recording condition $g_\pm$ as:

$$P(k|g_\pm) = \frac{N(k|g_\pm)}{\sum_k N(k|g_\pm)}$$

where $N(k|g)$ is the number of cells in cluster k with a particular recording condition g. An overall relative labelling statistic for each cluster was then computed by comparing conditional probabilities across recording values:

$$f_k = \frac{P(k|g_+)}{P(k|g_+) + P(k|g_-)}$$

Reaggregation experiments

Labelling, dissociation and reaggregation experiments (Figs. 4a–c, 5d,e and Extended Data Fig. 5c,d) were performed by recording Wnt activity in 96 haa gastruloids comprised of clonal Wnt-recorder cells as described earlier and immediately pooled into a 1.5 ml Eppendorf tube following completion of the 90 min recording window. The pooled samples were centrifugated, washed with 1 ml PBS and resuspended in 100 µl trypsin for dissociation. The samples were incubated at 37 °C for 5 min with occasional agitation to ensure complete dissociation. Trypsinization was then quenched with 200 µl N2B27 medium.

Gastruloids were reaggregated by two independent methods: 'bulk' and 'cytometer' based reaggregation. For bulk reaggregation, dissociated single-cell suspensions were resuspended in a volume of 190 µl N2B27 medium per gastruloid originally pooled, mixed thoroughly and replated into a fresh round-bottomed 96-well plate at 190 µl cell suspension per well to target a conserved total cell number per well. For cytometer reaggregation, dissociated single-cell suspensions were transferred to a cell sorter (Sony SH800), gated for single cells based on the light scattering profiles and then re-seeded into a 96-well plate at 1,000 single cells per well to initiate reaggregation. The samples were transferred to a tissue culture incubator to reaggregate and fixed and imaged for analysis. For bulk reaggregated samples, smaller 'satellite' aggregates formed in addition to primary aggregates. Satellite aggregates were excluded from analysis (Fig. 4c and Extended Data Fig. 5c,d).

Fusion and mosaic sorting experiments

Gastruloid fusion experiments (Fig. 6 and Extended Data Fig. 7) were performed from monoclonal spheroids seeded from $n = 200$ starting cells into low-attachment U-bottomed wells as described earlier. Previous to spheroid formation, all cells were cultured in 2i + LIF medium without dox. Spheroids were then aggregated into base N2B27 medium as described earlier or N2B27 medium supplemented with 2 µg ml^{-1} dox. Fusions were performed by manually transferring one spheroid (along with 10 µl medium) using a P20 pipette with a wide-bore pipette tip into the well of another spheroid and allowed to gravimetrically associate. For wild-type–wild-type fusion controls, two separate clonal cell lines expressing separate fluorescent proteins (P_{EF1a}–GFP or P_{PGK}–mCherry) were used.

For contact angle measurements, samples were aggregated for 24 h, transferred for fusion and fixed 3 h following transfer for imaging. For fusion gastruloid generation, the samples were aggregated for 48 h, following which they were transferred for fusion simultaneously with the addition of 3 µM CHIR and fed with CHIR-free medium at 72 haa according to the normal gastruloid generation protocol. Samples subjected to dox treatment conditions received continuous 2 µg ml^{-1} dox treatment for the duration of the experiment. The samples were fixed at 93 haa (that is, at 45 h after fusion).

Mosaic gastruloids were generated using a flow cytometer to sequentially seed 100 cells from each of two genetic backgrounds into each well of a 96-well low-attachment U-bottomed plate. Before mosaic spheroid formation all cells were cultured in 2i + LIF medium without dox. The spheroids were then aggregated into base N2B27 medium as described earlier or N2B27 media supplemented with 2 µg ml^{-1} dox. The samples were fixed at 24 haa for imaging.

Reaction-diffusion simulations

Reaction-diffusion pattern formation (Extended Data Fig. 5a,b) was modelled as a generic two-component system $q = (q_A, q_B)$ on a square two-dimensional lattice with periodic boundary conditions using custom MATLAB code. The system evolves according to the equation:

$$\frac{\partial q}{\partial t} = R(q) + D\nabla^2 q$$

where the reaction $R(q)$ models a simple 'activator–inhibitor' pair as:

$$R_A = r_1 q_A + r_2 q_B + k_A R_B = r_3 q_A + r_4 q_B + k_B$$

with coefficients $r_1 = 0.9$, $r_2 = -1$, $r_3 = 1$, $r_4 = -1.1$, $k_A = -0.025$ and $k_B = -0.025$. D is a diagonal matrix of diffusion coefficients $D_A = 1$ and $D_B = 12$. Parameters were tuned to capture a generic patterning instability; no direct correspondence to experimental measurements was presumed. Simulations were performed on a 50 × 50 lattice chosen such that spontaneous symmetry breaking forms a single pole. Simulations were initialized by independently initializing each pixel (i,j) to values

$$q_A^{ij} = 0.5 + \delta_A^{ij}$$

$$q_B^{ij} = 0.5 + \delta_B^{ij}$$

where δ_n^{ij} are normally distributed random variables with zero mean and variance (σ^2) = 0.0025. Simulations were evolved on a mesh size dt = 0.005. Representative images show scaled patterns of the activator q_A^{ij} at the time points of interest (Extended Data Fig. 5a).

Recording, dissociation and reaggregation simulations were modelled by first initializing a simulation and evolving until t_{dox} = 5 h, at which time distributed patches of activity are observed (qualitatively matching the pattern of Wnt activity in the 96 haa gastruloid). All cells above the median level of $q_A^{ij}(t_{dox})$ were then 'labelled' as Wnt recorded. Dissociation and reaggregation was simulated by subsequently randomizing the spatial indices i,j of all cells and continuing to time-evolve the reaction-diffusion dynamics for an additional 100 units until t_f = 105 h. At the conclusion, the posterior pole was identified according to location (i,j), which maximized $q_A^{ij}(t_f)$. Distances between simulation pixels and the posterior pole were calculated and binned (with unit bin width) to computer average pre-dissociation 'labelling' as a function of distance from final posterior pole. To compute the overall mean labelling profile, n = 100 independent simulations were run (Extended Data Fig. 5b).

Reporting summary

Further information on research design is available in the Nature Portfolio Reporting Summary linked to this article.

Data availability

The scRNAseq data generated in this study are available through the NCBI Gene Expression Omnibus (accession number GSE274389). Plasmids used to construct signalling-reporter and signalling-recorder cell lines are available from Addgene (plasmids 225522–225531). Source data are provided with this paper. All other materials (for example, cell lines) are available on request.

Code availability

The scRNAseq data were processed and analysed using the publicly available Single-Cell Analysis in Python (scanpy) software package version 1.10 and gastruloid images were processed using custom MATLAB code (MATLAB 2024a). All code is available on the authors' GitHub repository (https://github.com/toettchlab/McNamara2024).

References

57. Thielicke, W. & Sonntag, R. Particle image velocimetry for MATLAB: accuracy and enhanced algorithms in PIVlab. *J. Open Res. Softw.* **9**, 12 (2021).

Acknowledgements

The authors thank all members of the Toettcher laboratory, particularly E. Underhill, for their insightful comments and suggestions. We also thank A. Martinez-Arias for helpful discussions and feedback on the manuscript, K. Zaret for sharing reporter plasmid constructs, A. Lin for advice on single-cell sequencing and the Lewis Sigler Institute Genomics Core Facility team (W. Wang, J. Miller and J. A. Volmar) for technical support. Figure illustrations in Figures 1a, 2a, 4a, 6a,d,f,i and 7a,i were created in part using BioRender. This work was supported by the Lewis Sigler Scholars programme and the NSF Center for the Physics of Biological Function (grant number PHY1734030) to H.M.M., NIH (grant numbers T32GM007388 and F31HD113443) to S.C.S., NIH (grant number R35GM138167) to B.A., and NSF RECODE (grant number 2134935), NIH (grant numbers U01DK127429 and R01GM144362) and a Vallee Scholars award to J.E.T.

Author contributions

Conceptualization: H.M.M., M.M.C. and J.E.T. Methodology: H.M.M., S.C.S., M.M.C. and J.E.T. Investigation: H.M.M. Funding: H.M.M. and J.E.T. Writing and editing: H.M.M. and J.E.T. Supervision: J.E.T. and B.A.

Competing interests

J.E.T. is a scientific advisor for Prolific Machines and Nereid Therapeutics. B.A. is an advisory board member with options for Arbor Biotechnologies and Tessera Therapeutics, and holds equity in Celsius Therapeutics. H.M.M. is a cofounder and scientific advisor for C16 Biosciences. The remaining authors declare no conflicts of interest.

Additional information

Extended data is available for this paper at https://doi.org/10.1038/s41556-024-01521-9.

Supplementary information The online version contains supplementary material available at https://doi.org/10.1038/s41556-024-01521-9.

Correspondence and requests for materials should be addressed to Harold M. McNamara or Jared E. Toettcher.

Peer review information *Nature Cell Biology* thanks Takashi Hiiragi, Prisca Liberali and the other, anonymous, reviewer(s) for their contribution to the peer review of this work.

https://doi.org/10.1038/s41556-024-01521-9

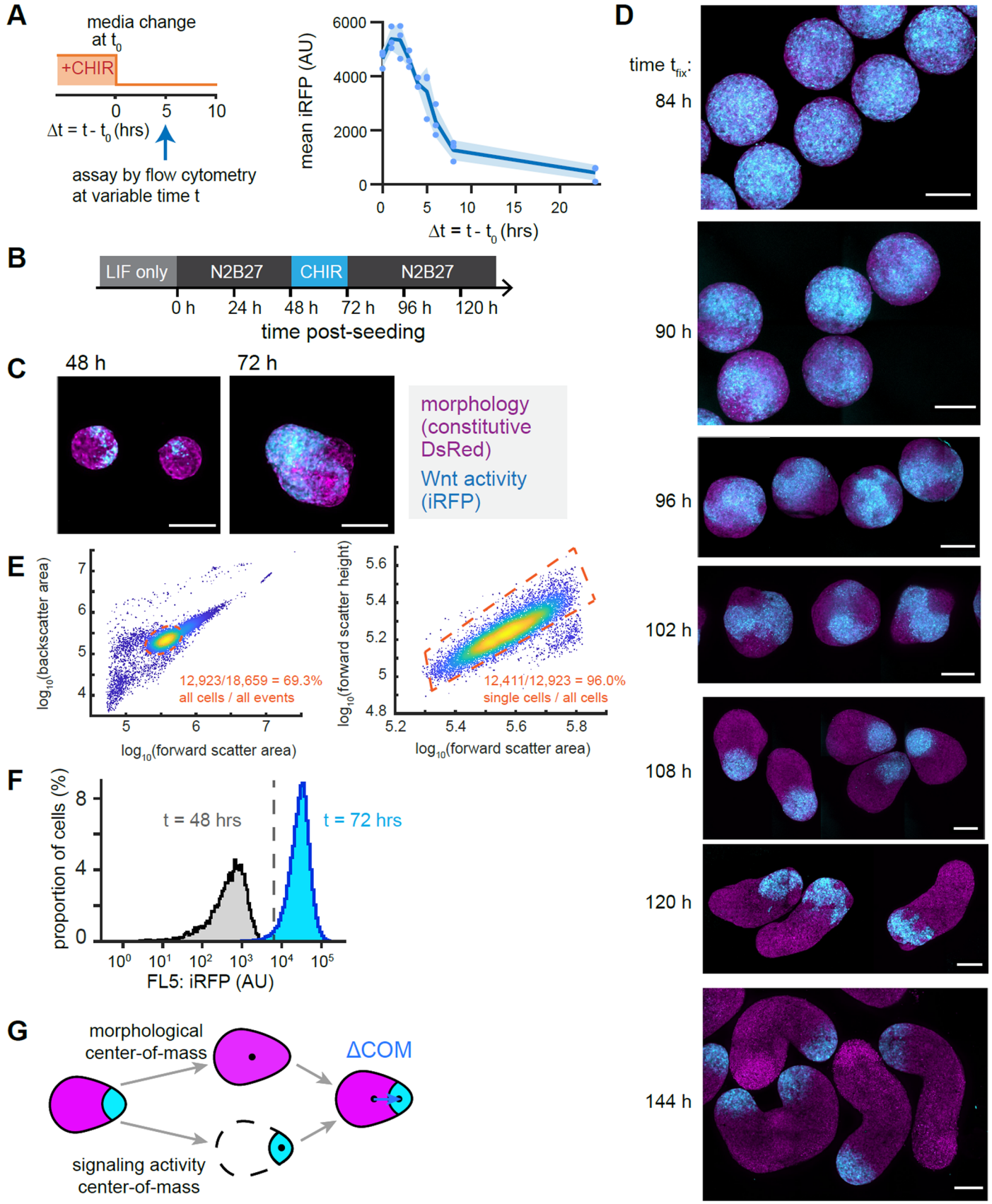

Extended Data Fig. 1 | See next page for caption.

https://doi.org/10.1038/s41556-024-01521-9

Extended Data Fig. 1 | Benchmarking the Wnt reporter during gastruloid development. (**A**) Characterization of off-kinetics of destabilized iRFP reporter of Wnt activity ($P_{TCF/LEF}$-iRFP-PEST). Shaded region indicates mean ± standard deviation. (**B**) Experimental protocol for gastruloid growth with 'LIF only' seed culture media. (**C**) Patterns of Wnt activity in gastruloids grown according to protocol in **B**. Wnt activity is heterogeneous both immediately before (t = 48 haa) and immediately after (t = 72 haa) CHIR treatment. Scale bar = 200 µm. (**D**) Representative images of Wnt activity patterns at different time points during polarization. Maximum-intensity projections are shown. Scale bar = 200 µm. (**E**) Representative data illustrating how single cells were gated for analysis from flow cytometry data (see Methods). (**F**) Definition of threshold to define Wnt-active versus Wnt-inactive cell populations (Fig. 1f) based on separation of activity distributions before (t = 48 haa) and after (t = 72 haa) CHIR stimulation. (**G**) Schematic of quantification of ΔCOM polarization metric (Fig. 1g).

https://doi.org/10.1038/s41556-024-01521-9

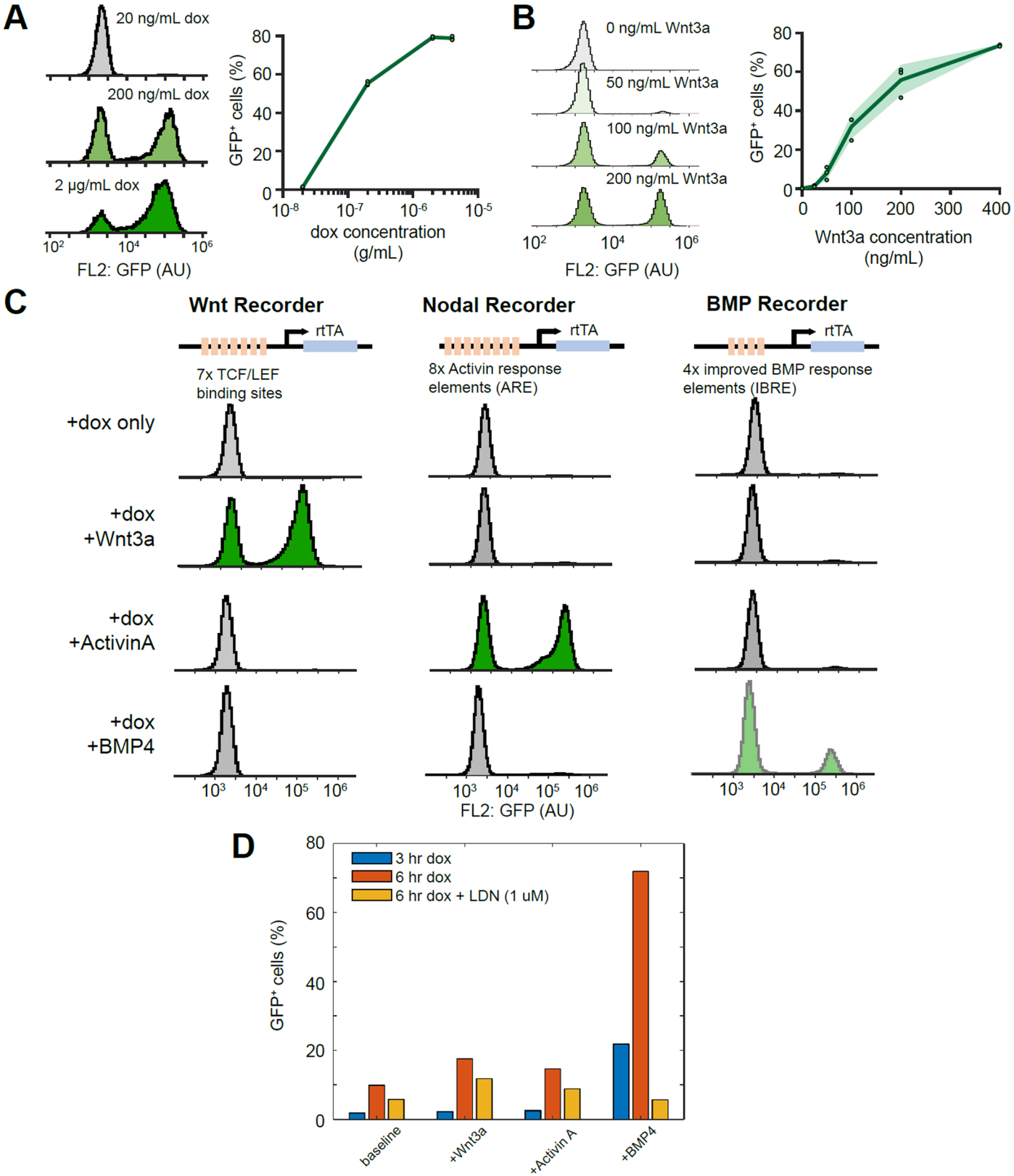

Extended Data Fig. 2 | Characterizing signal-recorder gene circuits. (**A**) Recording efficiency in Wnt-Recorder cells depends on doxycycline concentration (2i + LIF medium, 24 h recording window). (**B**) Recording efficiency in Wnt-Recorder cells depends on the concentration of recombinant Wnt3a ligand (200 ng ml^{-1} doxycycline, 24 h recording window). Shaded regions in (A-B) indicate mean ± standard deviation (3 biological replicates per condition). (**C**) Flow cytometry histograms corresponding to recorder-ligand crosstalk measurement in Fig. 2e. Recording windows were 6 h for Wnt Recorder and Nodal Recorder, and 3 h for BMP recorder. All ligand concentrations (including dox) were 200 ng ml^{-1}. (**D**) BMP-Recorder labelling is sensitive to BMP inhibition with LDN-193189.

https://doi.org/10.1038/s41556-024-01521-9

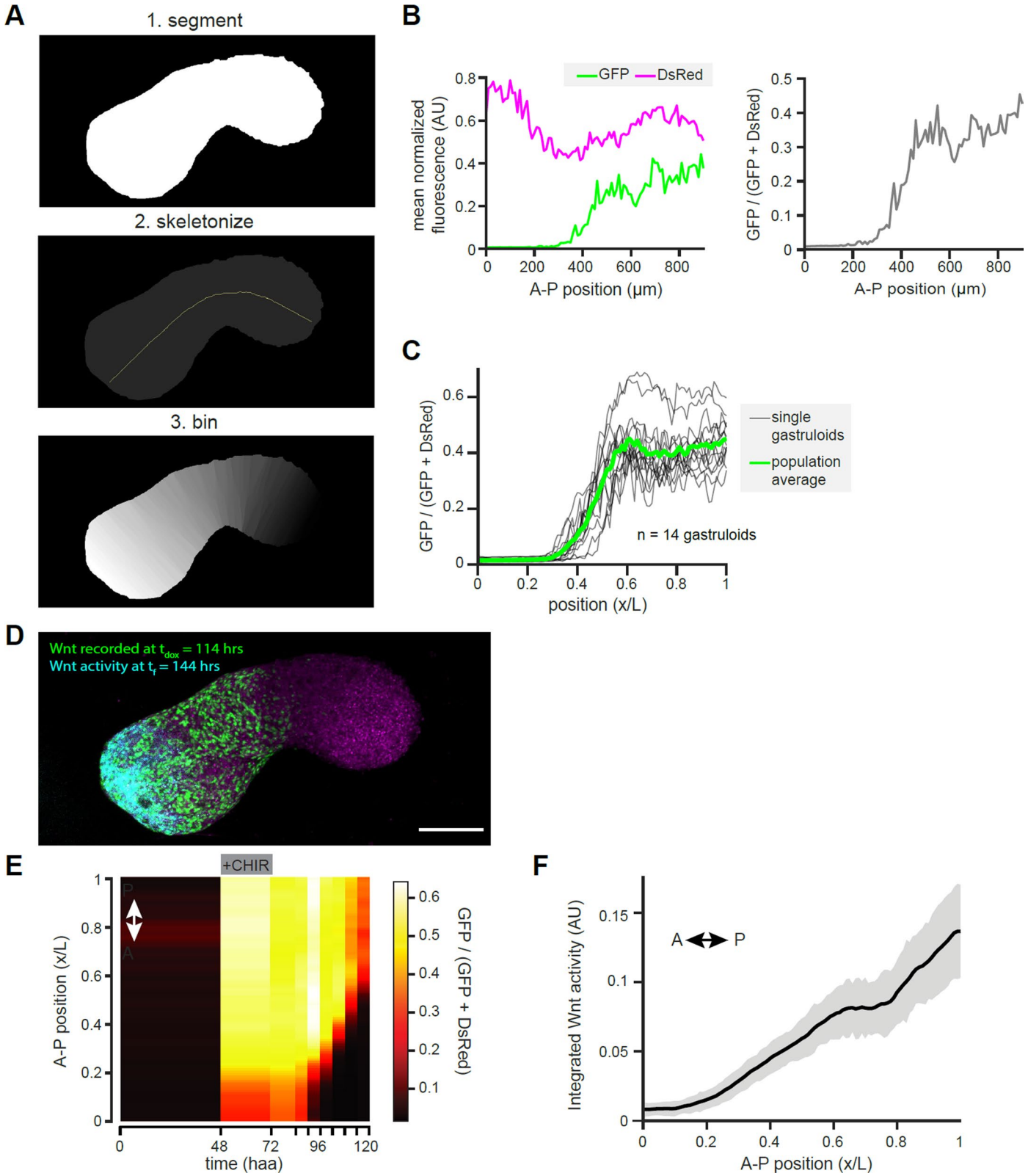

Extended Data Fig. 3 | See next page for caption.

https://doi.org/10.1038/s41556-024-01521-9

Extended Data Fig. 3 | Measuring positional information in signal-recorded gastruloids. (**A**) Illustration of image processing pipeline. Maximum-intensity projections of gastruloids are segmented, skeletonized, and then binned to assign an A–P coordinate to each pixel (Methods). (**B**) Left: Example quantification of average A–P profiles of both GFP and DsRed expression within a single gastruloid (t_{dox} = 114 h, t_f = 144 h). Pixel intensities were separately normalized relative to maximum image intensities in each channel. Right: relative fraction of GFP labelling across the A–P axis within the same gastruloid (Methods). (**C**) Overlay of relative fraction of GFP labelling in individual gastruloids for the same recording condition, along with the mean profile for this condition. (**D**) Simultaneous measurement of the final Wnt activity pattern and recorded Wnt activity signal within the same gastruloid. Maximum-intensity projection is shown. Scale bar = 200 µm. (**E**) Kymograph of the data presented in Fig. 3b to visualize different Wnt dynamics corresponding to different spatial positions. Following the emergence of an anterior domain at t_{dox} = 96 h, Wnt signalling becomes progressively more restricted to the posterior domain. (**F**) Integrated Wnt signalling activity between t = 96 and t = 134 h shows a linear 'temporal gradient' associated with A–P fate. Shaded regions indicate mean ± standard deviation as a function of A–P position.

https://doi.org/10.1038/s41556-024-01521-9

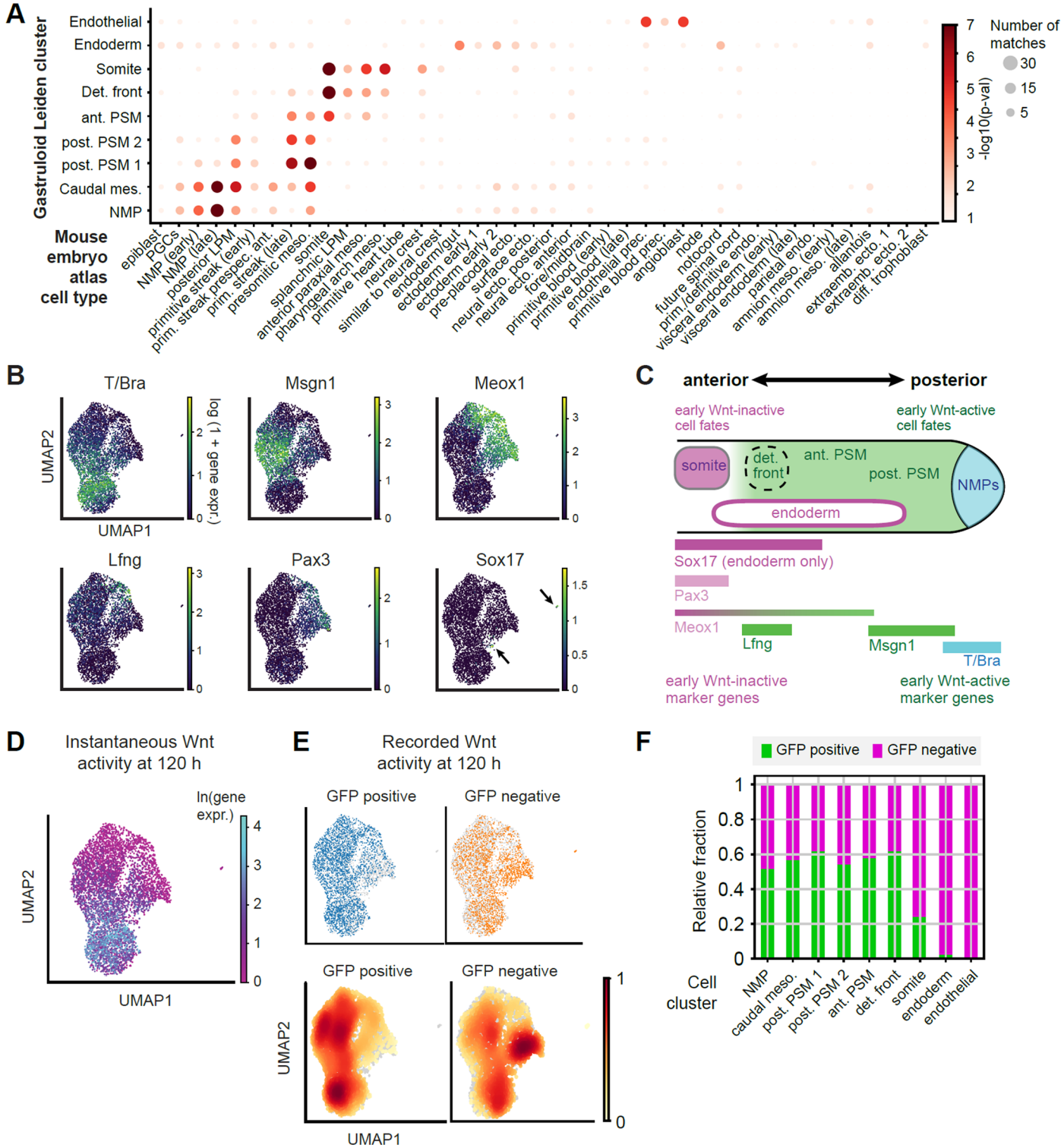

Extended Data Fig. 4 | Single-cell sequencing of 120 haa Wnt-recorded gastruloids. (**A**) Comparison of gene expression between Leiden clusters identified in gastruloids at t_{seq} = 120 h and annotated cell types from a reference atlas gene expression during mouse gastrulation[2]. Size of dots indicates the number of shared marker genes; colour indicates the binomial likelihood of having at least this many marker genes if compared to a random choice of marker genes (Methods). (**B**) Single-cell expression levels of reference genes associated with gastrulation and axial morphogenesis. (**C**) Illustration of reference gene organization across the anterior–posterior axis during axial elongation and somitogenesis. The organization of reference gene expression (Extended Data Fig. 4b) aligns with inferred histories of Wnt activity (Fig. 3c). (**D**) Final Wnt activity distribution across cells as measured by $P_{TCF/LEF}$-rtTA expression. (**E**) Top: individual cells in dataset separated according to Wnt-recording condition. Bottom: embedding density of cells according to Wnt-recording condition. (**F**) Relative contributions of GFP-positive and GFP-negative cells to different Leiden clusters, normalized according to total cells recovered in both conditions (Methods).

https://doi.org/10.1038/s41556-024-01521-9

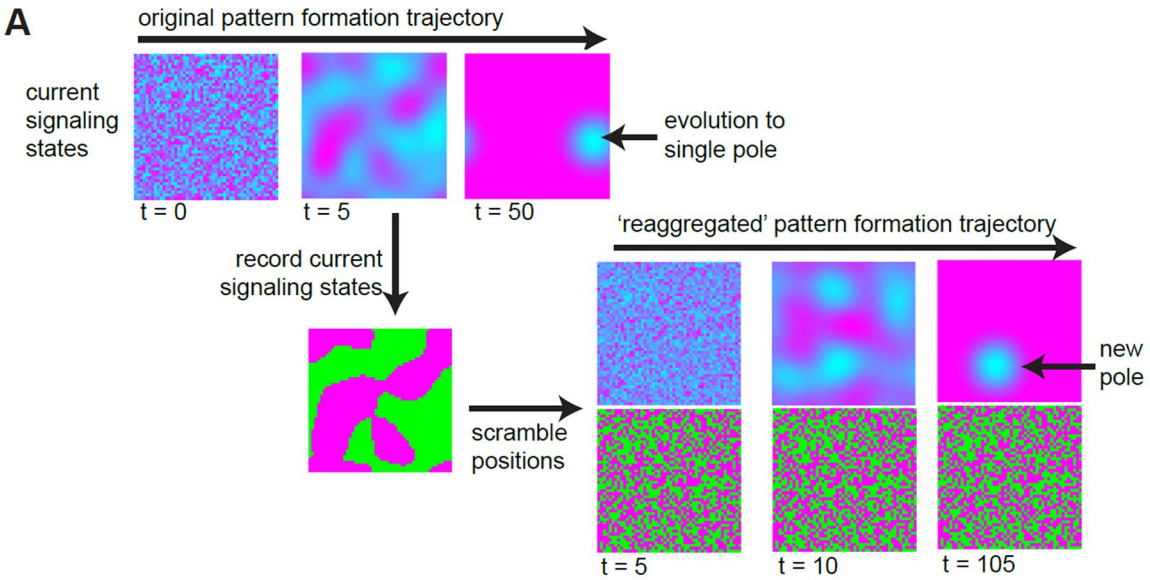

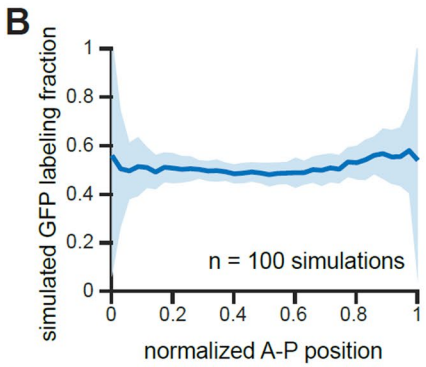

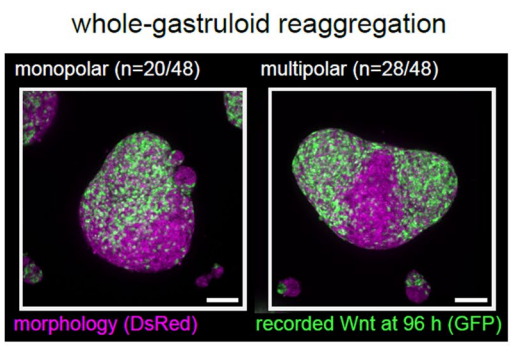

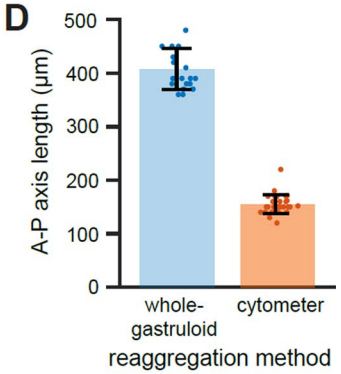

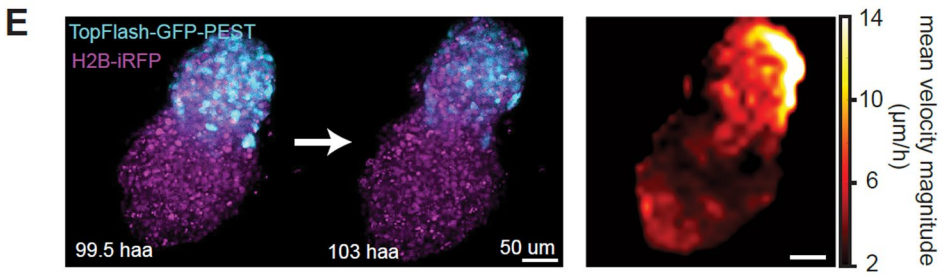

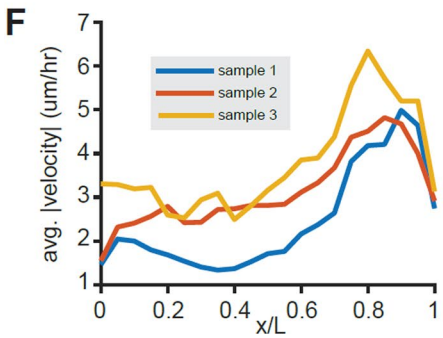

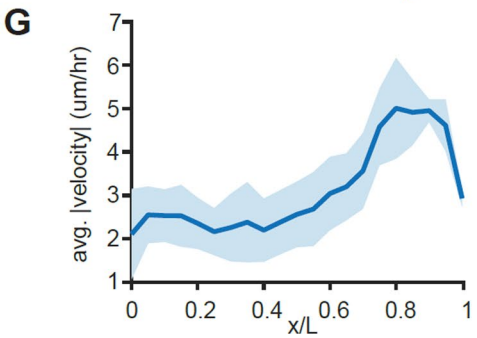

Extended Data Fig. 5 | See next page for caption.

https://doi.org/10.1038/s41556-024-01521-9

Extended Data Fig. 5 | Exploring Gastruloid reaggregation. (**A**) Computer simulation of signal-recording and dissociation/reaggregation experiment in the case of a reaction-diffusion Turing patterning circuit without cell rearrangements. Cell states are labelled according to signalling activity during an intermediate state, then cells locations are randomly shuffled (simulating dissociation), and continued to evolve according to the same reaction-diffusion equations. (**B**) Quantification of final A–P profiles of recording simulations under reaction-diffusion assumptions, averaged over n = 100 independent trials. Because a 'new' pole forms following reaggregation, recorded cells remain evenly distributed across the A–P axis. (**C**) Representative imaging of cell-sorting polarization following bulk reaggregation. n = 20 of 48 samples recovered show a single pole of Wnt-recorded cells (left). n = 28 of 48 show at least two poles of Wnt activity (right). Smaller 'satellite' clusters were not quantified. Maximum-intensity projections are shown. Scale bar = 100 µm. (**D**) Quantification of A–P axis length for reaggregated samples by flow cytometric sorting vs "bulk" reaggregation by pipetting cells into wells. Error bars indicate mean ± standard deviation. (**E**) Analysis of differential motility in polarized gastruloids. Left, Middle images: beginning and endpoint images of interval used to calculate motility. Right: average motility map, calculated using particle image velocimetry (PIV) on the nuclear iRFP channel. Motility was calculated for each frame, and then averaged to generate average motility maps (Methods). (**F**) A–P motility profiles for each of three biological replicates, calculated by averaging motility maps along the A–P axis. (**G**) Overall average A–P motility profile for all samples analysed. Shaded area represents mean ± standard deviation at each A–P position.

https://doi.org/10.1038/s41556-024-01521-9

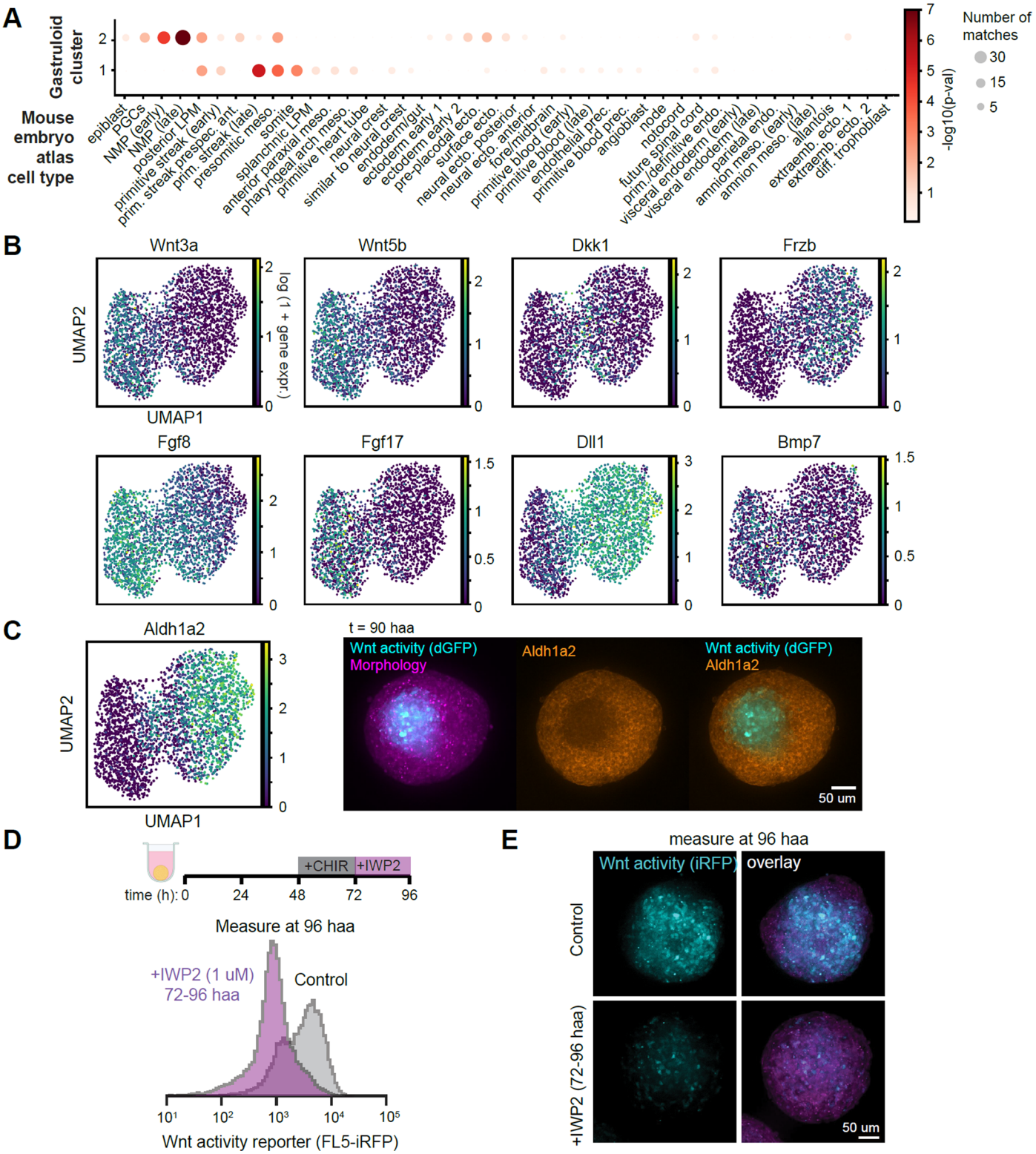

Extended Data Fig. 6 | Gene expression patterns in 96 haa Wnt-reporter gastruloids. (**A**) Comparison of gene expression between Leiden clusters identified in gastruloids at t_{seq} = 96 h and annotated cell types from a reference atlas gene expression during mouse gastrulation (Methods). Size of dots indicates the number of shared marker genes; colour indicates the binomial likelihood of having at least this many marker genes if compared to a random choice of marker genes (Methods). (**B**) Expression of signalling-associated genes within the scRNAseq dataset at t_{seq} = 96 h. (**C**) Expression of retinoic acid biosynthesis enzyme Aldh1a2 in the Wnt-inactive cell population. Maximum-intensity projections show, scale bar = 50 µm. (**D-E**) Positive feedback is required to maintain Wnt activity following cessation of CHIR treatment at 72 haa. (**D**) Flow cytometry measurements of single cell Wnt activity levels in dissociated gastruloids at 96 haa. Treatment with the inhibitor of Wnt secretion IWP-2 from 72 haa-onwards converts majority of cells to the Wnt-off population. (**E**) Imaging of Wnt activity patterns of intact gastruloids at 96 haa, with and without IWP-2 treatment. Maximum-intensity projections are shown. Scale bar = 50 µm.

https://doi.org/10.1038/s41556-024-01521-9

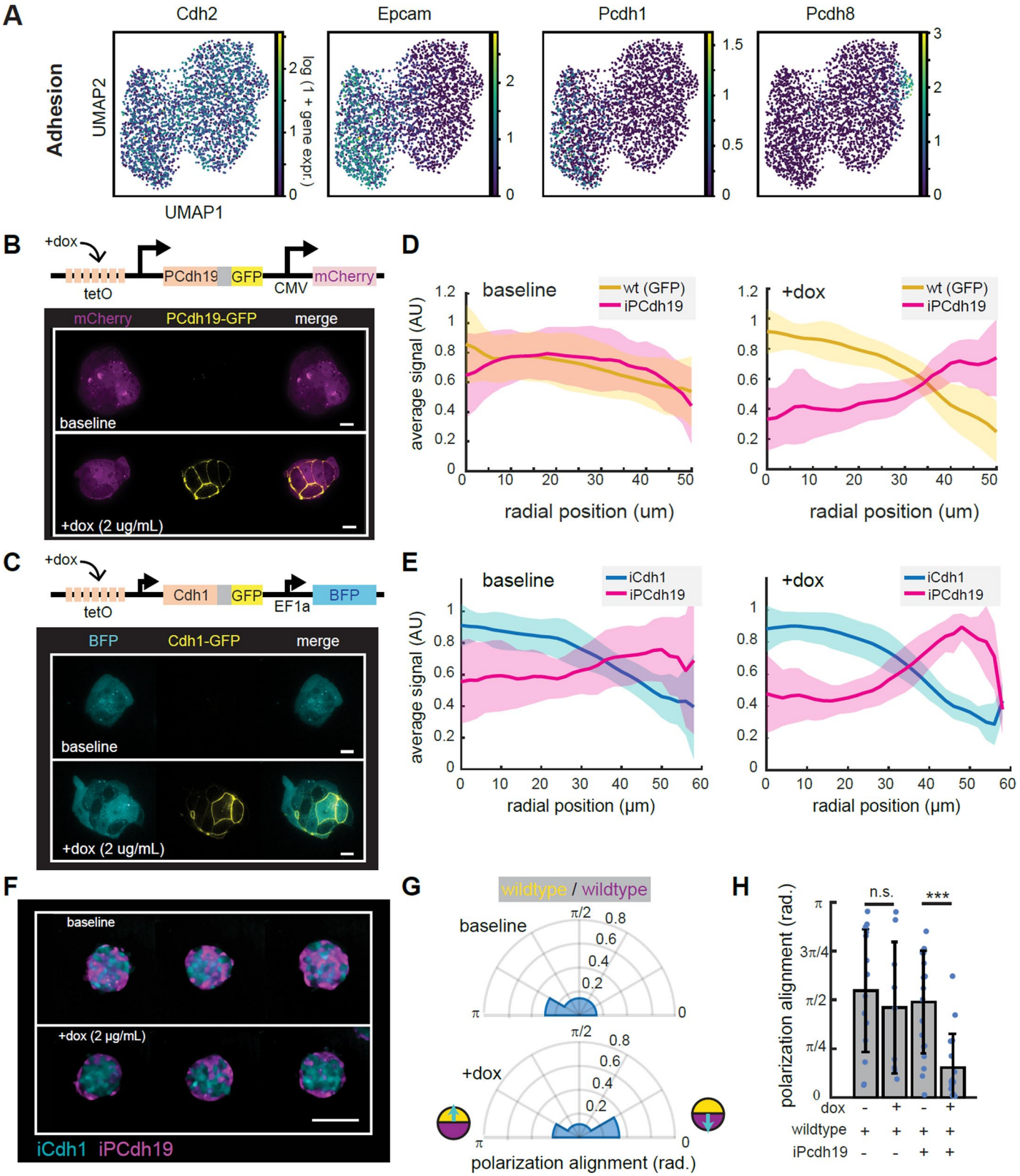

Extended Data Fig. 7 | Role of cell adhesion in gastruloid self-organization. (**A**) Single-cell differential expression of additional genes associated with cell–cell adhesion at 96 haa. (**B**) Doxycycline-dependent expression of Cdh1 within the iCdh1 cell line. Maximum-intensity projections shown, scale bar = 10 μm. (**C**) Doxycycline-dependent expression of Pcdh19 with the iPcdh19 cell line. Maximum-intensity projections shown, scale bar = 10 μm. Clones were chosen for similar expression levels upon induction. (**D-E**) Average radial concentrations of cell lines in mosaic spheroids with and without doxycycline treatment (related to Fig. 6h). N = 84 spheroids measured (Supplementary Table 3). Shaded regions indicate mean ± standard deviation. (**F**) Representative images of iCdh1/iPcdh19 mosaic spheroids. Maximum-intensity projections shown, scale bar = 100 μm. (**G**) Histogram of polarization alignment in fused gastruloids generated by fusing two wild-type spheroids, with and without doxycycline. (**H**) Quantification of average polarization alignment of fused spheroids in different conditions (related to Fig. 6l, Extended Data Fig. 7g). N = 58 gastruloids total (Supplementary Table 3). Conditions compared via two-sided *t*-test. P-values: p = 0.54, p = 0.00012. The asterisks (***) indicate p < 0.001.

https://doi.org/10.1038/s41556-024-01521-9

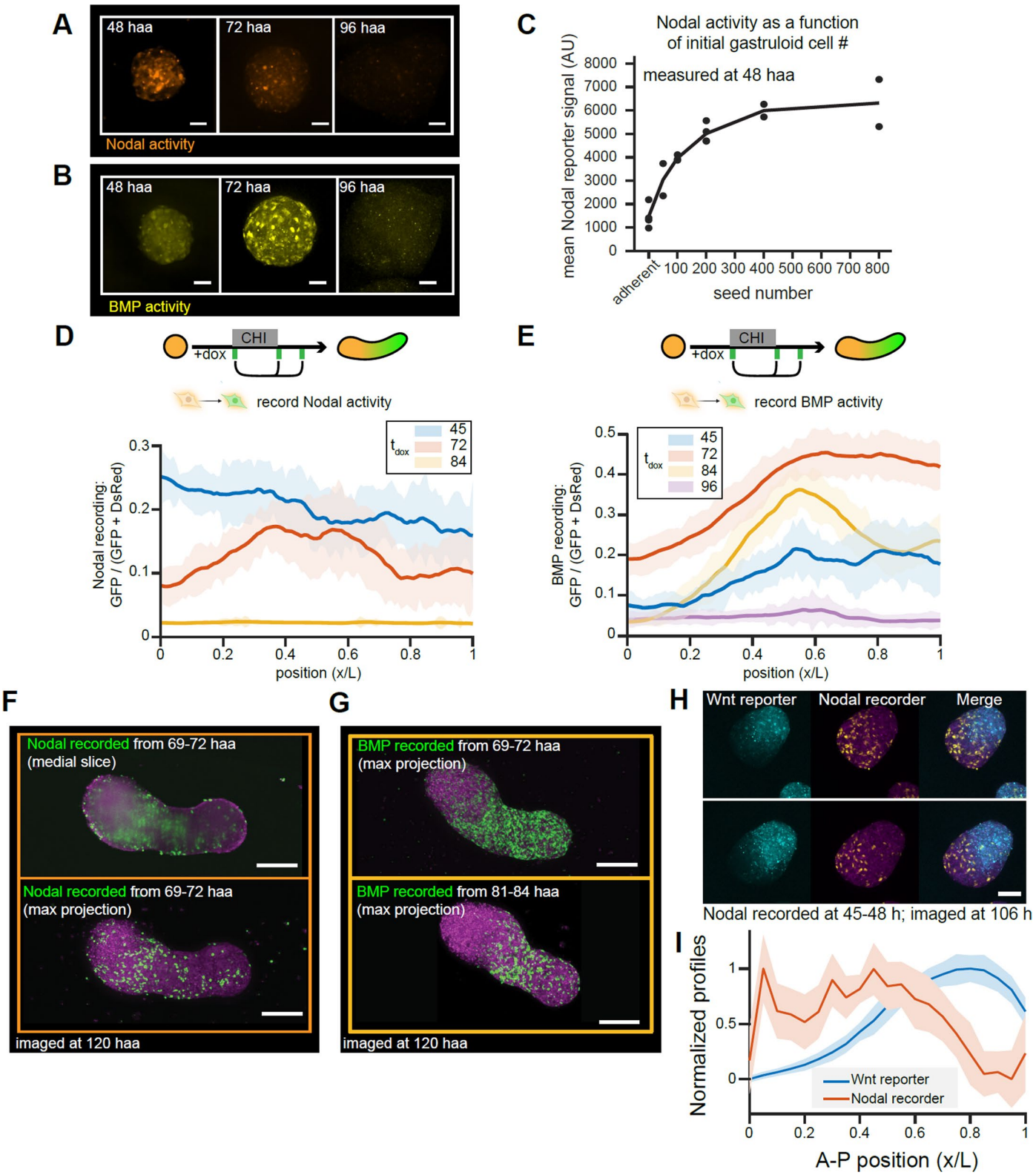

Extended Data Fig. 8 | See next page for caption.

https://doi.org/10.1038/s41556-024-01521-9

Extended Data Fig. 8 | Recording Nodal/BMP signalling during gastruloid self-organization. (**A**) Measurement of Nodal activity (PAR8-mCherry-PEST) at different time points during gastruloid development = . Maximum-intensity projections are shown, scale bar = 50 µm. (**B**) Measurement BMP activity (P_{IBRE4}-mCherry-PEST) at different time points during gastruloid development. Maximum-intensity projections are shown, scale bar = 50 µm. (**C**) Nodal activity levels in 48 haa gastruloids as a function of initial aggregate size. Nodal activity at 48 haa requires aggregation, and monotonically increases with aggregate size. Adherent cells were measured after 48 haa in equivalent media (N2B27) for comparison. (**D**) Recordings of early Nodal activity traced to t_F = 120 haa. (**E**) Recordings of early BMP activity traced to t_F = 120 haa. Shaded regions for C-D indicate standard deviation as a function of A–P position. N = 116 gastruloids measured total (Supplementary Table 3). (**F**) Representative image of spatial distribution of cell fates with recorded Nodal activity from 69-72 haa, imaged at 120 haa. Top: medial slice. Bottom: Maximum-intensity projection. Scale bar = 200 µm. (**G**) Representative images of cell fates with recorded BMP activity from 69-72 haa (top) and from 81-84 haa (bottom). Scale bar = 200 µm. Maximum-intensity projections are shown for both recording time points. (**H**) Simultaneous recording of early Nodal activity (recorded from 45-48 haa) and reporting of later instantaneous Wnt activity (imaged at 106 haa) in the same gastruloid using an engineered clonal cell line. Maximum-intensity projections of three separate representative gastruloids are shown. Scale bar = 100 µm. (**I**) Spatial distribution of early Nodal activity (recorded from 45-48 haa) traced to t_f = 120 haa, plotted alongside final Wnt activity. Normalized profiles are shown for comparison. Shaded region represents mean ± standard error of the mean for Nodal recording, and mean ± standard deviation for Wnt reporting. Nodal recording data from (**H**), plotted without normalization. Recording density varies approximately twofold along the A–P axis. N = 15 gastruloids measured.

https://doi.org/10.1038/s41556-024-01521-9

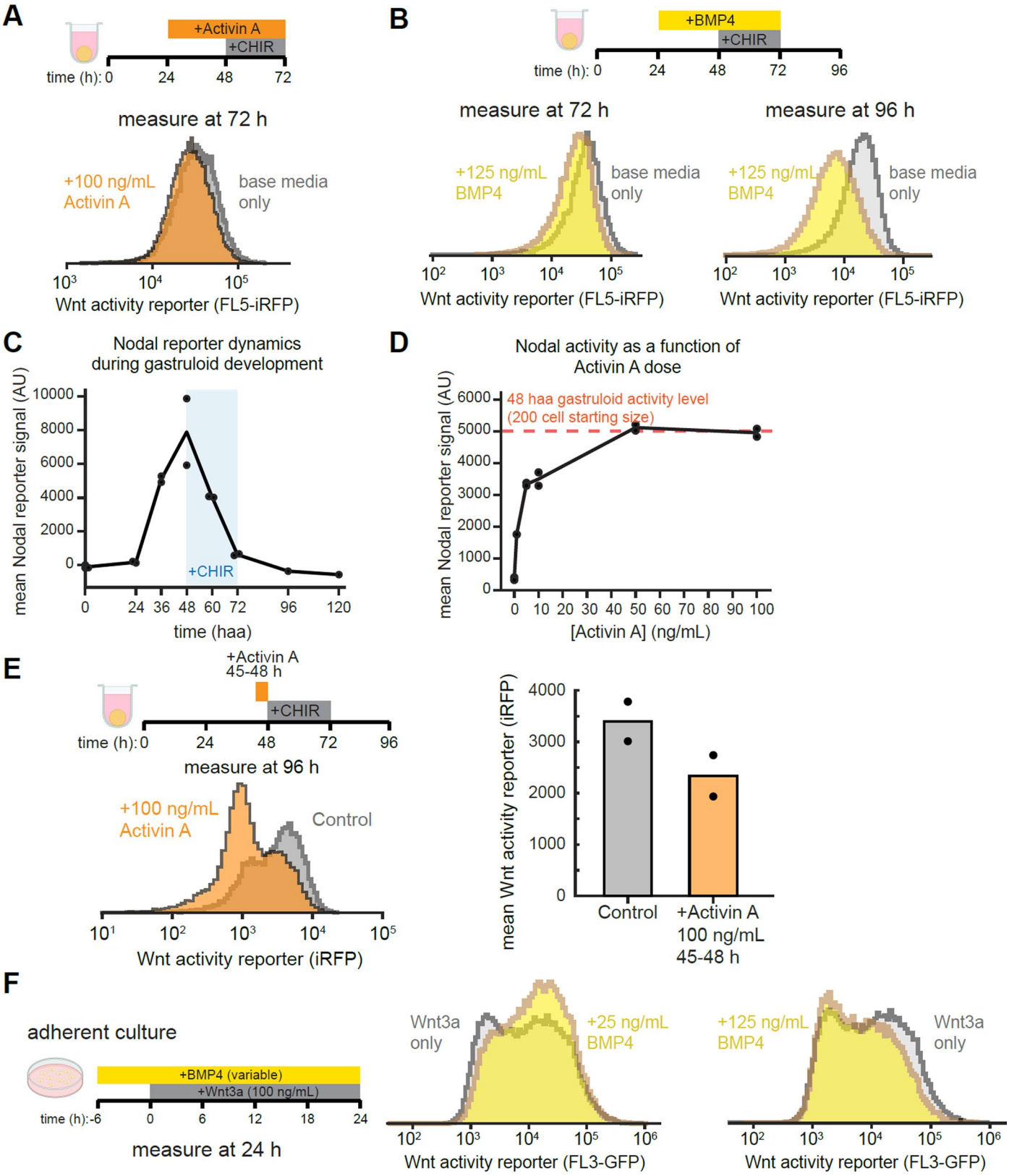

Extended Data Fig. 9 | See next page for caption.

https://doi.org/10.1038/s41556-024-01521-9

Extended Data Fig. 9 | Perturbing Nodal/BMP signalling during gastruloid self-organization. (**A**) Flow cytometry measurements of single-cell Wnt activity levels with and without Activin A pretreatment, measured at t = 72 h. (**B**) Flow cytometry measurements of single-cell Wnt activity levels with and without BMP4 pretreatment, measured at t = 72 h (left) and t = 96 h (right). (**C**) Dynamics of Nodal activity during gastruloid development, measured by flow cytometry of pooled and dissociated gastruloids. Substantial Nodal activity is detectable from 36-60, preceding CHIR stimulation at 48 and subsequently decaying to negligible levels by 72 h. (**D**) Nodal signalling levels in adherent cells treated for 48 h with different concentrations of recombinant Activin A (in N2B27). Dotted line is the mean gastruloid Nodal activity level at 48 haa under standard conditions (that is, initial aggregate of n = 200 cells) plotted for comparison. (**E**) Effect of a transient ActA treatment (100 ng ml^{-1}, applied from 45-48 haa) on Wnt activity levels at 96. Transient ActA treatment continues to cause an enrichment in Wnt-off cells at 96 haa, even when duration of treatment is reduced. (**F**) Co-treatment of adherent Wnt reporter cells with BMP4 affects responses to Wnt3a treatment. Whereas moderate BMP4 (25 ng ml^{-1}) treatment facilitated the Wnt response (middle), higher BMP4 (125 ng ml^{-1}) treatment suppressed the Wnt response.

https://doi.org/10.1038/s41556-024-01521-9

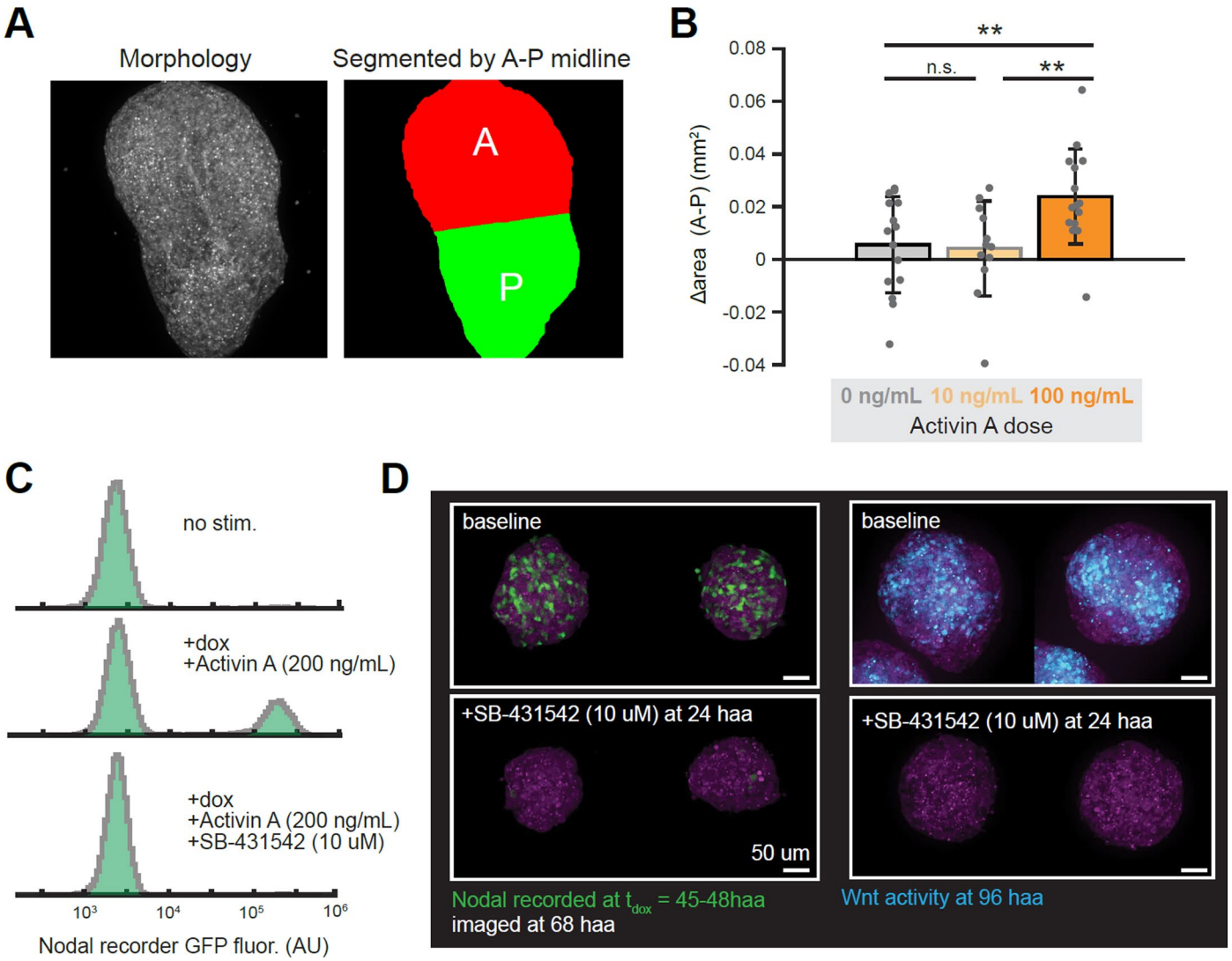

Extended Data Fig. 10 | Phenotypic consequences of Nodal perturbation. **A-B**). Quantification of anteroposterior morphology. (**A**) Gastruloid morphologies were segmented, binned according to nearest A–P axis coordinate (Methods, Extended Data Fig. 3), and then divided into anterior and posterior compartments based on the midline of the A–P axis (that is, without reference to Wnt activity). (**B**) Comparison of difference in area between anterior and posterior compartments under different Activin treatment conditions (that is, for samples analysed in Fig. 7g, h). 100 ng ml^{-1} Activin A treatment causes a morphological enlargement of the anterior compartment. N = 42 gastruloids measured (Supplementary Table 3). Statistical comparisons made via two-sided *t*-test; two asterisks (**) indicate p ≤ 0.01. P-values were: control and 10 ng ml^{-1} Activin, p = 0.84; control and 100 ng ml^{-1} Activin, p = 0.010; 10 ng ml^{-1} Activin and 100 ng ml^{-1} Activin, p = 0.0091. (**C**) Recording in the Nodal Recording cells is abolished with treatment with the Nodal inhibitor SB-431542. Activity was recorded for 3 h in 100 ng ml^{-1} doxycycline. (**D**) Endogenous early Nodal activity in gastruloids is abolished by Nodal inhibition from 24-48 haa. (Left) Nodal activity was recorded from 45-48 haa, with 100 ng ml^{-1} doxycycline, and measured at 68 haa. (Right) Early Nodal inhibition (from 24-48 haa) also abolished the formation of Wnt activity patches during symmetry breaking at 96 haa.

nature portfolio

Corresponding author(s): Jared Toettcher, Harry McNamara

Last updated by author(s): 8/9/2024

Reporting Summary

Nature Portfolio wishes to improve the reproducibility of the work that we publish. This form provides structure for consistency and transparency in reporting. For further information on Nature Portfolio policies, see our Editorial Policies and the Editorial Policy Checklist.

Statistics

For all statistical analyses, confirm that the following items are present in the figure legend, table legend, main text, or Methods section.

n/a	Confirmed
☐	☒ The exact sample size (*n*) for each experimental group/condition, given as a discrete number and unit of measurement
☒	☐ A statement on whether measurements were taken from distinct samples or whether the same sample was measured repeatedly
☐	☒ The statistical test(s) used AND whether they are one- or two-sided *Only common tests should be described solely by name; describe more complex techniques in the Methods section.*
☒	☐ A description of all covariates tested
☒	☐ A description of any assumptions or corrections, such as tests of normality and adjustment for multiple comparisons
☐	☒ A full description of the statistical parameters including central tendency (e.g. means) or other basic estimates (e.g. regression coefficient) AND variation (e.g. standard deviation) or associated estimates of uncertainty (e.g. confidence intervals)
☐	☒ For null hypothesis testing, the test statistic (e.g. *F*, *t*, *r*) with confidence intervals, effect sizes, degrees of freedom and *P* value noted *Give P values as exact values whenever suitable.*
☒	☐ For Bayesian analysis, information on the choice of priors and Markov chain Monte Carlo settings
☒	☐ For hierarchical and complex designs, identification of the appropriate level for tests and full reporting of outcomes
☒	☐ Estimates of effect sizes (e.g. Cohen's *d*, Pearson's *r*), indicating how they were calculated

Our web collection on statistics for biologists contains articles on many of the points above.

Software and code

Policy information about availability of computer code

Data collection	Imaging data was collected using NIS Elements version 4.40.00 (Nikon Inc). Cell sorting was performed using the Sony SH800 cell sorter (Sony Inc; no version number). No other software was used in data collection.
Data analysis	Image analysis was performed in ImageJ 1.54f and MATLAB R2024a. Single-cell sequencing data were processed and analyzed using the publicly available Single-Cell Analysis in Python (scanpy version 1.10) software package. All code is available on authors' Github repository (www.github.com/toettchlab/McNamara2024).

For manuscripts utilizing custom algorithms or software that are central to the research but not yet described in published literature, software must be made available to editors and reviewers. We strongly encourage code deposition in a community repository (e.g. GitHub). See the Nature Portfolio guidelines for submitting code & software for further information.

Data

Policy information about availability of data

All manuscripts must include a data availability statement. This statement should provide the following information, where applicable:

- Accession codes, unique identifiers, or web links for publicly available datasets
- A description of any restrictions on data availability
- For clinical datasets or third party data, please ensure that the statement adheres to our policy

Single-cell RNA sequencing data generated in this study is available through the NCBI Gene Expression Omnibus (GEO) (accession number GSE274389). Plasmids

used to construct signaling-reporter and signaling-recorder cell lines are available from Addgene (plasmids #225522-225531). All numerical data in the paper is available as Source Data. All other materials (e.g., cell lines) are available upon request.

Research involving human participants, their data, or biological material

Policy information about studies with human participants or human data. See also policy information about sex, gender (identity/presentation), and sexual orientation and race, ethnicity and racism.

Reporting on sex and gender	N/A
Reporting on race, ethnicity, or other socially relevant groupings	N/A
Population characteristics	N/A
Recruitment	N/A
Ethics oversight	N/A

Note that full information on the approval of the study protocol must also be provided in the manuscript.

Field-specific reporting

Please select the one below that is the best fit for your research. If you are not sure, read the appropriate sections before making your selection.

☒ Life sciences ☐ Behavioural & social sciences ☐ Ecological, evolutionary & environmental sciences

For a reference copy of the document with all sections, see nature.com/documents/nr-reporting-summary-flat.pdf

Life sciences study design

All studies must disclose on these points even when the disclosure is negative.

Sample size	No statistical methods were used to pre-determine sample sizes; sample sizes were designed to be similar to those reported in recent publications (Beccari et al, Nature 2018; Merle et al, Nat Struct Mol Biol 2024).
Data exclusions	A small proportion of gastruloids (<10%) failed to elongate (consistent with field standards for gastruloid reproducibility; see Turner et al, Development 2017) and were excluded from anterior-posterior profile analysis (Fig. 3B, 7D-G, S8D-E). For bulk gastruloid reaggregation experiments (Fig. 4C; Fig. S5C-D), very small satellite ES cell aggregates and multipolar aggregates were excluded from analysis of A-P profiles.
Replication	All experiments were performed in at least two biological replicates to ensure reproducibility. All attempts at replication were successful.
Randomization	No randomization was performed because no covariates were present in the basic molecular and cell biology performed here.
Blinding	No blinding was performed because all experiments were conducted by a single experimental biologist.

Reporting for specific materials, systems and methods

We require information from authors about some types of materials, experimental systems and methods used in many studies. Here, indicate whether each material, system or method listed is relevant to your study. If you are not sure if a list item applies to your research, read the appropriate section before selecting a response.

Materials & experimental systems

n/a	Involved in the study
☐	☒ Antibodies
☐	☒ Eukaryotic cell lines
☒	☐ Palaeontology and archaeology
☒	☐ Animals and other organisms
☒	☐ Clinical data
☒	☐ Dual use research of concern
☒	☐ Plants

Methods

n/a	Involved in the study
☒	☐ ChIP-seq
☐	☒ Flow cytometry
☒	☐ MRI-based neuroimaging

Antibodies

Antibodies used	anti-Pcdh19 (Abcam ab191198), anti-Aldh1a2 (Abcam ab156019), anti-Cdh1 (Cell Signaling Technology 3195T), Goat anti-rabbit Alexa647 (Invitrogen A27040), anti-Brachyury (R&D Systems, AF2085).
Validation	We used well established commercial antibodies from reputable vendors that have also been used in prior publications (e.g., Pcdh19: Wu et al, Mol Brain 2021; Cdh1: extensive validation on Cell Signaling website and 3,000+ citations; Brachyury: 100+ citations).

Eukaryotic cell lines

Policy information about cell lines and Sex and Gender in Research

Cell line source(s)	E14tg2a mouse embryonic stem cell line, obtained directly from ATCC for this paper.
Authentication	Cell line was not independently authenticated, but is authenticated in-house at ATCC by STR profiling.
Mycoplasma contamination	Lines were tested and confirmed negative for mycoplasma (ATCC Universal Mycoplasma Kit 30-1012K).
Commonly misidentified lines (See ICLAC register)	None.

Plants

Seed stocks	N/A
Novel plant genotypes	N/A
Authentication	N/A

Flow Cytometry

Plots

Confirm that:

☒ The axis labels state the marker and fluorochrome used (e.g. CD4-FITC).

☒ The axis scales are clearly visible. Include numbers along axes only for bottom left plot of group (a 'group' is an analysis of identical markers).

☒ All plots are contour plots with outliers or pseudocolor plots.

☒ A numerical value for number of cells or percentage (with statistics) is provided.

Methodology

Sample preparation	Methods are described in the Supplementary Methods, from which the following is quoted: To assess gastruloids via flow cytometry, at least n = 30 gastruloids were first pooled into a 1.5 mL Eppendorf tube, centrifugated (500 rcf, 3 min), washed in PBS, and then trypsinized in 100 µL of TrypLE Express at 37 °C. Gastruloids were trypsinized for 3 minutes, retrieved and triturated to dislodge gastruloids, and returned to 37 for an additional 3 minutes to complete digestion. Trypsinization was then quenched with 300 µL of N2B27, after which samples were immediately assayed via flow cytometry. Cytometer events were first gated for events corresponding to cells based on forward scattering and backscattering profiles, and then for single cells based on the height and area of forward scattering events (Fig. S1D).
Instrument	Sony SH800 fluorescence-activated cell sorter
Software	Sony standard flow cytometry software
Cell population abundance	Because we worked with a single cell line, 100% of cell events corresponded to the relevant cell population.
Gating strategy	Cells were gated on size and shape (forward scatter / backscatter) and doublets were discriminated using forward scatter height vs area. See Fig. S1E.

☒ Tick this box to confirm that a figure exemplifying the gating strategy is provided in the Supplementary Information.